Two Birds with One Stone: One-pot Concurrent Ta-doping and -coating on Ni-Rich $LiNi_{0.92}Co_{0.04}Mn_{0.04}O_2$ Cathode Materials with Fiber-type Microstructure and Li^+-conducting Layer Formation

Yola Bertilsya Hendri[a], Liang-Yin Kuo[a,b], Manojkumar Seenivasan[a], Yi-Shiuan Wu[a], She-Huang Wu[a,c], Jeng-Kuei Chang[d], Rajan Jose[e], Martin Ihrig[g], Payam Kaghazchi[h,i], Chun-Chen Yang[a,b,f]∗

[a]*Battery Research Center of Green Energy, Ming Chi University of Technology, Taishan, New Taipei City, 24301, Taiwan*

[b]*Department of Chemical Engineering, Ming Chi University of Technology, Taishan, New Taipei City, 24301, Taiwan*

[c]*Graduate Institute of Science and Technology, National Taiwan University of Science and Technology, 43, Sec. 4, Keelung Road, Taipei 106, Taiwan*

[d]*Department of Materials Science and Engineering, National Yang Ming Chiao Tung University, 1001 University Road, Hsinchu, 30010, Taiwan*

[e]*Nanostructured Renewable Energy Materials Laboratory, Faculty of Industrial Sciences and Technology, University Malaysia Pahang, 26300 Kuantan, Malaysia*

[f]*Department of Chemical and Materials Engineering, and Green Technology Research Center, Chang Gung University, Taoyuan City 333, Taiwan*

[g]*Department of Chemical Engineering, National Taiwan University of Science and Technology, No. 43, Keelung Rd., Sec. 4, Da'an Dist., Taipei City 106335, Taiwan*

[h]*Institute of Energy and Climate Research, Materials Synthesis and Processing (IEK-1) Forschungszentrum Jülich GmbH, 52428 Jülich, Germany*

[i]*MESA+ Institute for Nanotechnology, University of Twente, 7500 AE Enschede, the 16 Netherlands*

GRAPHICAL ABSTRACT

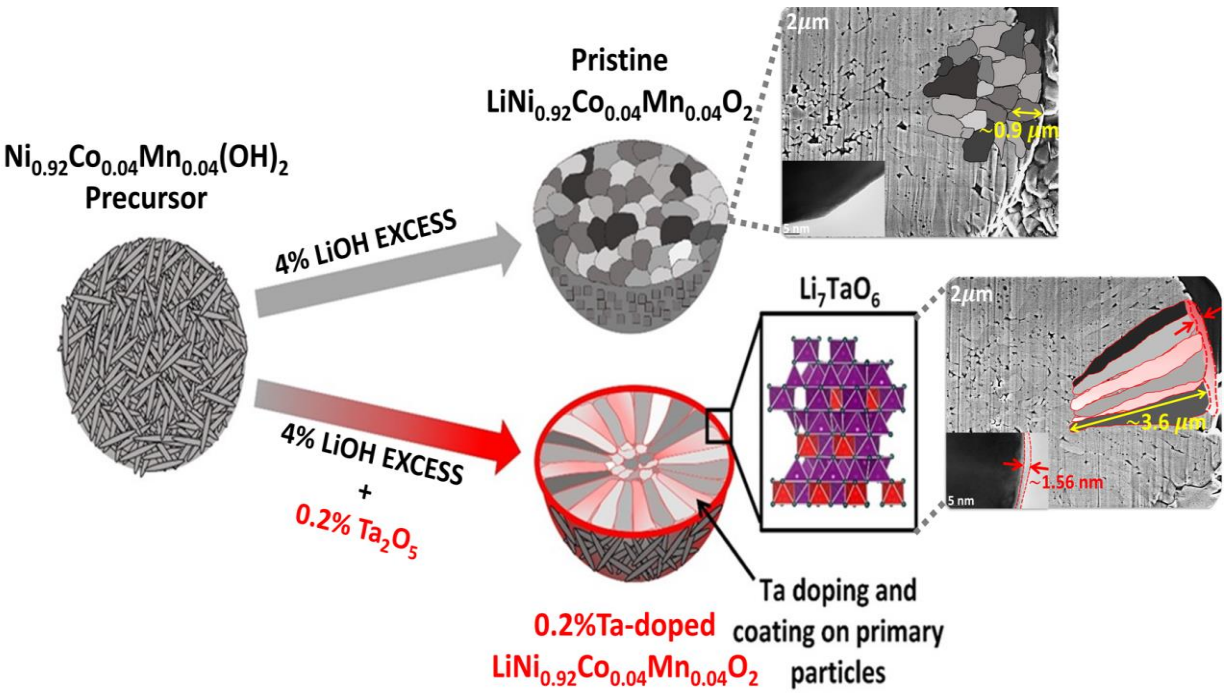

ABSTRACT

A novel scalable Taylor–Couette reactor (TCR) synthesis method was employed to prepare Ta-modified $LiNi_{0.92}Co_{0.04}Mn_{0.04}O_2$ (T-NCM92) with different Ta contents. Through experiments and density functional theory (DFT) calculations, the phase and microstructure of Ta-modified NCM92 were analyzed, showing that Ta provides a bifunctional (doping and coating at one time) effect on $LiNi_{0.92}Co_{0.04}Mn_{0.04}O_2$ cathode material through a one-step synthesis process via a controlling suitable amount of Ta and Li-salt. Ta doping allows the tailoring of the microstructure, orientation, and morphology of the primary NCM92 particles, resulting in a needle-like shape with fine structures that considerably enhance Li^+ ion diffusion and electrochemical charge/discharge stability. The Ta-based surface-coating layer effectively prevented microcrack formation and inhibited electrolyte decomposition and surface-side reactions during cycling, thereby significantly improving the electrochemical performance and long-term cycling stability of NCM92 cathodes. Our as-prepared NCM92 modified with 0.2 mol% Ta (i.e., T2-NCM92) exhibits outstanding cyclability, retaining 84.5% capacity at 4.3 V, 78.3% at 4.5 V, and 67.6% at 45℃ after 200 cycles at 1C. Even under high-rate conditions (10C), T2-NCM92 demonstrated a remarkable capacity retention of 66.9% after 100 cycles, with an initial discharge capacity of 157.6 mAh g^{-1}. Thus, the Ta modification of Ni-rich NCM92 materials is a promising option for optimizing NCM cathode materials and enabling their use in real-world electric vehicle (EV) applications.

Keywords: Ni-rich NCM, Taylor-Couette Reactor, NCM optimization, Ta modified, DFT simulation

1. Introduction

Lithium-ion batteries (LIBs) play a crucial role in energy storage and have been extensively employed in various areas such as consumer electronics, electric vehicles (EVs), and hybrid electric vehicles (HEVs) [1–4]. However, the constant need for reliability, high safety, low cost, high energy and power densities, long cycle life, and excellent rate performance requires further improvement of LIBs, particularly, that of the cathode active materials [1].

Cathode active materials are the main components that determine the electrochemical performance, safety, and cost of LIBs [1,5,6]. Based on their structure, cathode active materials can be categorized as layered (e.g., $LiCoO_2$, NCM333, NCM523, NCM622, and NCM811), spinel ($LiMn_2O_4$), olivine ($LiFePO_4$), and tavorite materials with different structures (e.g., $LiVO(PO_4)$, $LiV(PO_4)F$, and $LiFe(SO_4)F$) [7,8]. Among them, Ni-rich Li $[Ni_xCo_yMn_{1-x-y}]O_2$ ($x > 0.9$) cathode active materials are ideal candidates for future commercial applications because of their high reversible discharge capacities, high energy density, relatively low material cost, and environmentally benign nature, owing to their low Co content [9]. Unfortunately, increasing the Ni content of Ni-rich cathode materials results in detrimental cycling instability and severe safety issues, particularly at high temperatures and working voltages. The fading mechanisms of Ni-rich $Li[Ni_xCo_yMn_{1-x-y}]O_2$ (with $x > 0.9$) materials can be summarized as follows: cation mixing disorder triggered by the material preparation process and extensive cycling, residual lithium compounds formed owing to secondary reactions that also cause the oxygen evolution reaction (OER), microcracking of particles, rock-salt impurity phase formation, dissolution of transition metal ions, structure degradation, and structure decay [6,10–12]. In addition, safety issues due to the increased nickel concentration also hinder its further commercialization. The high-nickel formulations increase the amount of unstable Ni^{4+}, which induces fast reduction reactions during thermal decomposition with subsequent exothermic oxygen release, leading to thermal runaway in the battery [13,14].

Numerous attempts have been made to enhance the cycling and thermal stabilities of Ni-rich cathode active materials [1,3,5,10,14–16], such as introducing foreign cations and anion dopants into the crystal lattice for structural stabilization of the host materials (known as doping) [2,10,17], protective surface layer coatings to prevent HF attack from the decomposed electrolytes [1,10], improving synthesis techniques [10,18], and developing concentration-gradient microstructures. Surface coating and foreign ion doping are two widely used strategies for improving the structural stability of Ni-rich cathode active materials, including metal cations and anions, and coating materials such as fluorides, phosphates, fast ion conductors, and metal oxides have been reported in the literature [2]. H.H. Sun *et al.* studied $LiNi_{0.91}Co_{0.09}O_2$ cathode materials doped with various cation dopants, such as Mn^{2+}, Al^{3+}, Ti^{4+}, Ta^{5+}, and Mo^{6+} [19]. They claimed that the electrochemical performance of Ni-rich cathode materials featuring dopants with high oxidation states (Ta^{5+} and Mo^{6+}) significantly outperformed their counterparts featuring dopants with low oxidation states (Mg^{2+} and Al^{3+}). They showed that Li^+ ion pouch cells with Ta^{5+}-and Mo^{6+}-doped LNCO cathodes retained 81.5% capacity at 200 mA g^{-1} for 3000 cycles. Recently, Zhang reported that all problems related to the intrinsic properties of Ni-rich cathode materials are due to residual lithium compounds and the thermal instability of the H2–H3 phase transition [20]. No single approach capable of solving all these problems is currently available, and several strategies are required.

Recent reports indicate that achieving a better cycling performance in highly nickel-rich cathode active materials requires precise control of the microstructure of the particles [21]. The radially oriented primary particles limit the stress in the radial direction, allowing the secondary particles to shrink and expand during the charging/discharging process without causing significant stress along the grain boundaries between the particles. Park *et al.* reported that doping with boron cations could change the microstructure of the primary particles to become increasingly thinner and elongated in the radial direction, thus achieving improved capacity retention of 91% after 100 cycles at 55 ℃ [22]. Nguyen *et al.* demonstrated that Sn doped into

$Li[Ni_{0.90}Co_{0.05}Mn_{0.05}]O_2$ particles provides thin and elongated primary particles that are tightly packed and free of voids; therefore, they can exhibit a good capacity retention of 92.9% after 100 cycles at 4.3 V [23]. Nevertheless, it has been reported that not all dopant elements can effectively alter the orientation and morphology of primary NCM-based particles [18,24]. Among the other dopants, Ta is a promising highly Ni-rich cathode active material [2,7]. Ta exhibits the highest transition metal–oxygen (TM−O; here Ta–O bond) bond dissociation energy value to oxygen (BDEO) at 839 kJ mol^{-1}, along with a high ionic radius and oxidation state of Ta^{5+} [25]. These properties may inhibit Ni^{2+} ion migration from the TM sites to Li sites, reduce the number of Jahn-Teller active Ni^{3+} ions, and alter the lattice structure of the cathode active material, thereby affecting the electrochemical behavior. Jamil *et al.* synthesized $LiNi_{0.88}Co_{0.09}Al_{0.03}O_2$ (NCA88) doped with a 1 wt.% Ta. It showed an excellent cycling capacity retention performance of ~93% at 1C for 100 cycles and 75% capacity retention at a high voltage of 4.5 V at 1C for 100 cycles [26].

In addition, the type of synthesis method affects the physical properties of cathode material, such as primary and secondary particle size and shape, crystallinity, and size distribution as well as electrochemical performance [5,27]. In this study, we applied a co-precipitation method using a novel scalable Taylor–Couette reactor (TCR) to synthesize $Ni_{0.92}Co_{0.04}Mn_{0.04}(OH)_2$ hydroxide precursors. The TCR provides a flow characteristic in which fluid flows between two cylinders (e.g., internal and external cylinders) in the direction of rotation. TCR reactor delivers strong and homogeneous radial mixing with a small axial dispersion. As the rotation speed of the inner cylinder reaches a critical value, it develops a vortex rotating in opposite directions along the axis, called a Couette-Taylor vortex. This Couette-Taylor vortex induces highly effective radial mixing within each vortex cell and uniform fluidic motion enabling enhanced mass transfer and facilitates mixing. In this way, the TCR reactor allows very homogeneous micro-mixing with higher mixing intensity, shorter processing times, highly uniform spherical particles, narrow size distribution, and fast reaction

kinetics. Therefore, unlike other reactor types (e.g., continuous stirred-tank reactors (CSTRs)), the TCR reactor can provide spherical secondary particles with tiny flakes of primary particles, thereby enhancing the electrochemical performance of $LiNi_{0.92}Co_{0.04}Mn_{0.04}O_2$ (NCM92) cathode active materials. Furthermore, we studied the Ta-modification of NCM92 using TCR synthesis. To date, no reports exist in the literature on the preparation of Ni-rich NCM92 materials with Ta dopant based on NCM92 hydroxide precursors via TCR. To understand the role of Ta in detail, we combined experimental results and density functional theory (DFT) calculations. Our results indicate that Ta substitution into NCM92 not only changes the microstructure, orientation, and morphology of the primary particles into radially aligned needle-like fine structures but also forms a coating layer on the Ta-modified NCM92 particle surface. Thus, the Ta-based modifications of NCM92 significantly improved its electrochemical performance and long-term cycling stability. We like to highlight again no report yet in literature by using a single doping element in Ni-rich cathode material (particularly, for Ni content is over 92% with Ta), showing a bifunctional (doping and coating at one time) effect on Ni-rich NCM cathode material through a one-step synthesis process via a simple controlling suitable amount of Ta and Li-salt. DFT calculation result also confirmed our experimental findings. The same concept can be applied to the other Ni-rich cathode material to do property modification.

2. Experimental Section

***2.1Synthesis of P-NCM92 and Tx-NCM92 Materials*:** $LiNi_{0.92}Co_{0.04}Mn_{0.04}O_2$ was fabricated via a facile co-precipitation approach using a Taylor–Couette reactor (TCR) (LCTR®-tera 3100, Laminar Co., LTD, Korea), followed by a solid-state reaction under suitable sintering conditions. A 2 M mixed metal salt solution (aq.) of nickel sulfate hexahydrate ($NiSO_4 \cdot 6H_2O$) (Thermo Scientific, 98%), cobalt sulfate heptahydrate ($CoSO_4.7H_2O$) (Sigma Aldrich, 99%), and manganese sulfate monohydrate ($MnSO_4 \cdot H_2O$) (J.T. Baker, 98%) at a Ni: Co: Mn molar

ratio of 92:4:4 was prepared. In addition, 4 M NaOH (aq.) (J.T. Baker, 98%), and 8 M ammonium hydroxide (aq.) (Honeywell, ≥ 25% NH_3 in H_2O) were also prepared to control the pH and act as precipitant and chelating agents, respectively. All the solutions were simultaneously pumped into the TCR. The temperature and pH level of the reactor were maintained throughout the reaction at 60 ℃ and 11.2, respectively. The precipitated powder was collected, washed with deionized (DI) water and ethanol, and then dried at 80 ℃ for 6 h. The as-prepared $Ni_{0.92}Co_{0.04}Mn_{0.04}(OH)_2$ powders and $LiOH.H_2O$ (molar ratio of 1:1.04) were mixed using the dry ball mill method for 2 h and then calcined at 745 ℃ for 15 h under pure O_2 atmosphere to form pristine-$LiNi_{0.92}Co_{0.04}Mn_{0.04}O_2$ (denoted as P-NCM92) powders. To prepare Ta-modified $LiNi_{0.92}Co_{0.04}Mn_{0.04}O_2$ (denoted as Tx-NCM92), the $Ni_{0.92}Co_{0.04}Mn_{0.04}(OH)_2$ powders and $LiOH.H_2O$ were mixed with appropriate amounts of tantalum (V) oxide (Ta_2O_5) (Sigma Aldrich, 99%) and calcined at the same condition as P-NCM92. The amounts of Ta-modification varied from 0.1, 0.2, 0.3, and 1 mol%, denoted as T1-NCM92, T2-NCM92, T3-NCM92, and T10-NCM92, respectively.

***2.2 Materials Characterizations*:** The chemical states of the elements in the P-NCM92 and Tx-NCM92 cathode active materials and the electrode before and after cycling were investigated using XPS (PHI5600, PerkinElmer, U.S.A.), and the data were analyzed using XPSPEAK 4.1 software. The particle morphologies and structures of the as-prepared powders were studied using SEM (Hitachi S–2600H, Japan), FE-SEM (JEOL JSM-7610F Plus, Japan) with EDS, and HR-TEM (JEOL JEM–2100F, Japan). A focused ion beam (FIB; FEI Helios G4 UX) was used to study the prepared cross sections of the P-NCM92 and Tx-NCM92 particles. The pore sizes of P-NCM92 and T2-NCM92 were verified using the Brunauer–Emmett–Teller (BET) method (Micromeritics Gemini VII 2390 Series, USA). The particle sizes and particle distribution of the prepared P-NCM92 and T2-NCM92 were examined using a LS 13 320 dynamic light scattering (DLS) particle size analyzer (Beckman Coulter, USA). The variation in the crystal structure with the intercalation/deintercalation of Li^+ ions of the cathode was measured in real-

time by applying a current (0.1C with a voltage window of 2.8–4.3 V (*vs.* Li/Li^+)) to the coin cell while repeatedly measuring the XRD patterns. The crystallinity of the prepared P-NCM92 and Tx-NCM92 cathode active material and electrodes before and after cycling were validated by XRD (Bruker D2 PHASER, Germany; Cu Kα5; λ = 0.1534753 nm; 30 kV, 10 mA). The lattice parameters were determined by the Rietveld refinement method with the TOPAS manufacturer (V. 4.2). The relationship between full width at half maximum (FWHM) and crystallite size was explained by the Scherrer equation [28].

$$\tau = \frac{K\lambda}{\beta \cos\theta}$$

Where, τ is the crystallite size; K is a dimensionless shape factor (0.9); λ is the X-ray wavelength (1.54□); β is the full width at half maximum (FWHM) of the peak; and θ is the Bragg angle.

***2.3 Theoretical methods*:** Spin-polarized DFT calculations were performed using the Projector Augmented-Wave (PAW) [29] pseudopotential method implemented in the Vienna Ab initio Simulation Package (VASP) code.[30] The Perdew–Burke–Ernzerhof (PBE) [31] functional was employed to approximate the exchange-correlation (XC) energy for all DFT calculations of atomistic structures. A 6 × 6 × 1 supercell ($Li_{108}Ni_{108}O_{216}$, $Li_{100}Ni_{107}Ta_1O_{216}$, and $Li_{99}Ni_{106}Ta_2O_{216}$) was used to model pristine and Ta-modified $LiNiO_2$ (LNO) structures. A 1 × 1 × 1 *k*-point mesh was applied to all Ta-modified LNO structures. Ta_2O_5 and Li_7TaO_6 oxide materials were obtained from the Crystallography Open Database (COD) and Materials Project (MP) database. They were modeled using 1 × 1 × 1 unit cells (Ta_4O_{10} and $Li_{21}Ta_3O_{18}$) with *k*-point meshes of 3 × 3 × 3 (Ta_2O_5) and 2 × 2 × 1 (Li_7TaO_6). The oxygen molecules were modeled using a 20 × 20 × 20 supercell with a 1 × 1 × 1 *k*-point mesh. The grain boundary (GB) calculations were performed for two distinct GBs: GB1 ($\Sigma2[\bar{1}\bar{1}20]/(1\bar{1}0\bar{4})$) with 96 atoms and GB2 ($\Sigma3[110]/(1\bar{1}02)$) with 192 atoms. These GBs were modeled by a 2 × 1 × 1 and 2 ×

2×1 k-point mesh, respectively. An energy cutoff of 600 eV as well as an energy and force convergence criterion of 10^{-4} and 10^{-3} eV $Å^{-1}$ was used for all calculations. The atomic structures were visualized using VESTA.[32]

***2.4 Cell Fabrication*:** The positive electrode was prepared by mixing the cathode active material, conductive Super-P, and polyvinylidene fluoride (80:10:10 weight ratio) in N-methylpyrrolidone (NMP). The slurry was coated onto a carbon-coated Al foil current collector with a loading level of 2–3 mg cm^{-2}, then dried in an oven at 60 °C overnight in an air atmosphere. The positive electrode was assembled into a coin-type half-cell (CR2032) in an Ar-filled glove box, using Li metal as the anode and a microporous polyethylene (PE) membrane (Celgard 2400) as the separator. The electrolyte consisted of a solution of 1 M $LiPF_6$ in ethylene carbonate (EC) and diethyl carbonate (DEC) (1:1, v/v; Aldrich). Subsequently, the coin-type half-cell was sealed and used for electrochemical measurements.

***2.5 Electrochemical performance measurements*:** The electrochemical charge and discharge tests were performed at a rate of 1C (200 mA g^{-1}) within 2.8–4.3 V or 4.5 V (*vs.* Li/Li^+) at 30 and 45 °C using a BCS-805 workstation (Bio-Logic, France). The electrochemical workstation (PGSTAT302N; Metrohm Autolab B. V., the Netherlands) was used to conduct CV (scan rate at 0.01 mV s^{-1} and scanning voltage of 2.8–4.5 V (*vs.* Li/Li^+)). CV and EIS (PGSTAT302N; Metrohm Autolab B. V., the Netherlands) were used to study the redox electrochemical reaction and interface impedance (frequency range of 100 kHz–0.01 Hz with an amplitude of 5 mV), respectively. The galvanostatic intermittent titration technique (GITT) was conducted at a 0.1C constant current of charging/discharging for 10 min, with a relaxation time of 40 min between 2.8 and 4.3 V using the P-NCM92 electrode and T2-NCM92 electrode with the mass loading were 2.41 mg cm^{-2} and 2.97 mg cm^{-2}, respectively.

2.6 Post-mortem analysis: The electrode morphology and particle cross section before and after cycling were investigated using SEM (Hitachi S–2600H, Japan) and a FIB (FEI Helios G4 UX),

respectively. HR-STEM, SAD, and EDS mapping of the NCM92-based electrodes after long-term cycling (after 200 cycles at 1C/1C) were investigated using a high-resolution transmission electron microscope (JEOL JEM-2100F, Japan). The preparation procedures of the TEM thin-film samples for micrometer-sized NCM92 powder particles consist of three main steps: (1). the selected particles were covered by focused ion beam (FIB) Pt coating to avoid preparation-induced damage and retain nanoscale thin-film features after the Ar-ion bombardments, then (2). the electron-transparency cross sections of the ion-milled particles from the surface to core portions with uniform-thickness strips were thinned by FIB, and (3). the TEM thin-film samples were finally transferred to a carbon film-supported copper grid for HR-STEM-SAD-EDX analyses by a glass needle mounted on a micromanipulator.

3. Results and Discussion

The microstructure of primary particles is essential for mitigating the failure mechanism and tailoring the electrochemical properties and performance of highly Ni-rich layered oxide cathode active materials. This study provides new insights into modifying the microstructure of $LiNi_{0.92}Co_{0.04}Mn_{0.04}O_2$ (NCM92) using Ta-based modifications. The effects of Ta incorporation on the microstructure, morphology, physical and electrochemical properties of the NCM92 cathode active materials were evaluated in detail. Therefore, we analyzed pristine $LiNi_{0.92}Co_{0.04}Mn_{0.04}O_2$ (denoted as P-NCM92) and Ta-modified $LiNi_{0.92}Co_{0.04}Mn_{0.04}O_2$ (denoted as Tx-NCM92, x=1, 2, 3, 10), in which the Ta-content varied from 0.1, 0.2, 0.3, and 1 mol%, and denoted as T1-NCM92, T2-NCM92, T3-NCM92, and T10-NCM92, respectively.

3.1. Structural analysis of Ta-modified NCM92

The structural properties of P-NCM92 and Tx-NCM92 were analyzed using X-ray powder diffraction (XRD), as shown in Fig. 1. The diffraction peaks of all P-NCM92 and Tx-NCM92 samples can be easily indexed to the typical layered hexagonal $R\bar{3}m$ space group of α-$NaFeO_2$ (JCPDS card No. 87-1562). No peaks associated with the Ta-based compounds were

detected. The explicit splitting of the (006)/(102) and (108)/(110) peaks demonstrates that all the samples possessed a highly ordered layered structure and that Ta modification did not significantly alter the internal structure of the NCM92 crystal. Table S1 and Fig. S1 show Rietveld refinement results of the P-NCM92 and Tx-NCM92 samples. The results demonstrated a slight expansion in the lattice parameters *a* and *c* and the cell volumes after Ta modification. This lattice expansion can be explained by the larger Ta^{5+} ion radius than those of Mn^{3+}, Ni^{3+}, and Co^{3+} (Ta^{5+} (0.649 Å) > Mn^{3+} (0.580 Å) > Ni^{3+} (0.560 Å) > Co^{3+} (0.545 Å)). Thus, the expansion of the lattice parameters and cell volumes with a larger Ta content indicates substitution at the TM sites. In addition, the ratio of $I_{(003)}/I_{(104)}$ peaks reduced upon increasing the amount of Ta dopant (Table S1), which indicates increased cation mixing as the incorporation of Ta dopants increases, as confirmed by the value of Ni^{2+}/Li^{+} in 3b sites (Table S1). This phenomenon correlated with the existence of Ta^{+5} at the TM sites, which induced the reduction of the Ni^{3+} into Ni^{2+} (confirmed by X-ray photoelectron spectroscopy (XPS) results, Fig. 4a) to maintain the electroneutrality of the lattice, and caused the Ni^{2+} to partially occupy the Li sites owing to the similar ionic radius (Li^{+} = 0.76 Å and Ni^{2+} = 0.69 Å) [33], as shown in Table S1 [21]. The full width at half maximum (FWHM) of the (003) peak increased with increasing Ta modification, implying that the crystallite size decreased progressively with increasing Ta concentration (Table S1). Furthermore, the thickness of the TM-O_2 slab and Li-O_2 inter-slab are determined by using the lattice parameter (*c*) and the oxygen ion's coordinate (Z_{ox}) and are presented in Table S1 [33–35]. The T2-NCM92 has the lowest TM-O_2 slab thickness and highest Li-O_2 inter-slab space thickness compared to other samples, presumably owing to the occupancies of Li^{+} and Ni^{+} ion in the layered structure and the cation mixing, thus altering the distance of the TM-O_2 and Li-O_2 [33–35]. A high Li-O_2 inter-slab space thickness of T2-NCM92 compared to other samples might reduce the migration energy barrier of the Li^{+} ions, facilitate structural stability, and enhance the Li^{+} ion transportation during charge/discharge [26,33,36].

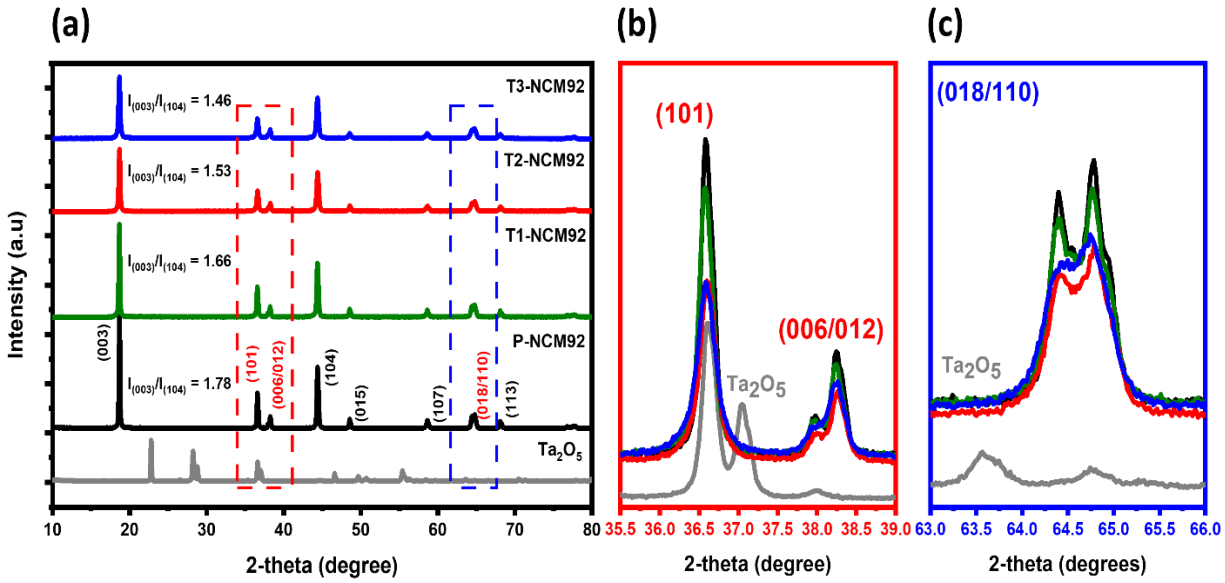

Fig. 1. (a). XRD patterns of the P-NCM92 and Tx-NCM92 at different Ta modification amounts, (b). Magnification of the (101) and (006/012) peaks, (c). Magnification of the (018/110) peaks.

3.2. Microstructural analysis of Ta-modified NCM92

Fig. S2 shows the morphology of the $Ni_{0.92}Co_{0.04}Mn_{0.04}(OH)_2$ precursor prepared using the novel scalable Taylor–Couette Reactor (TCR) and commercially available $Ni_{0.8}Co_{0.1}Mn_{0.1}(OH)_2$ precursor synthesized using the CSTRs reactor [37]. The as-prepared $Ni_{0.92}Co_{0.04}Mn_{0.04}(OH)_2$ precursors exhibited a unique morphology (The TCR needle-like precursor was completely different from the CSTR precursor, which exhibited a granular-shaped morphology with a wider particle size distribution). However, our precursors consisted of homogeneously tiny primary flake-like particles and spherical secondary particles. The particle size distribution and XRD patterns of the TCR-$Ni_{0.92}Co_{0.04}Mn_{0.04}(OH)_2$ precursors and commercially available CSTRs-$Ni_{0.8}Co_{0.1}Mn_{0.1}(OH)_2$ precursors are shown in Fig. S3 and S4, respectively. The average particle size (D_{50}) of the TCR-$Ni_{0.92}Co_{0.04}Mn_{0.04}(OH)_2$ was *ca.* 6.8 µm, which is larger than that of commercially available CSTRs-$Ni_{0.8}Co_{0.1}Mn_{0.1}(OH)_2$ (*ca.* 5.5 µm). The XRD spectra of both samples were indexed to the layered hexagonal-$Ni(OH)_2$ crystal structure (JCPDS:14-0117) and showed that both samples were in a pure phase [38]. However, the intensity ratio of $I_{(101)}/I_{(001)}$ for the TCR-$Ni_{0.92}Co_{0.04}Mn_{0.04}(OH)_2$ was higher than that of

commercially available CSTRs-$Ni_{0.8}Co_{0.1}Mn_{0.1}(OH)_2$, indicating the growth rate of (101) was faster than (001) and the preferential growth trend of (101) crystal plane was observed in TCR-$Ni_{0.92}Co_{0.04}Mn_{0.04}(OH)_2$ [39,40]. In addition, inductively coupled plasma optical emission spectroscopy (ICP-OES) results revealed that the chemical composition of Ni, Co, and Mn in the $Ni_{0.92}Co_{0.04}Mn_{0.04}(OH)_2$ sample was close to the nominal Ni:Co:Mn atomic ratio of 92:4:4, confirming that the precursor was successfully synthesized with the correct composition.

The $LiNi_{0.92}Co_{0.04}Mn_{0.04}O_2$ cathode active materials were synthesized by mixing as-prepared TCR-$Ni_{0.92}Co_{0.04}Mn_{0.04}(OH)_2$ precursor with LiOH and then heating to 745 ℃ for 15 h. Fig. S5 and S6 display the scanning electron microscopy (SEM) and energy dispersive spectroscopy (EDS) results of P-NCM92 and Tx-NCM92. The morphology of Tx-NCM92 differed slightly from that of P-NCM92. The primary particles of the P-NCM92 sample were shorter and wider than those of the Tx-NCM92 sample, which were much longer and thinner. Although there are microstructure changes, the Ni, Co, and Mn elements are homogeneously distributed in P-NCM92 and Tx-NCM92 (Figure S6). Importantly, the EDS results confirmed the presence of the Ta elements in all the Tx-NCM92 samples, as shown in Fig. S6.

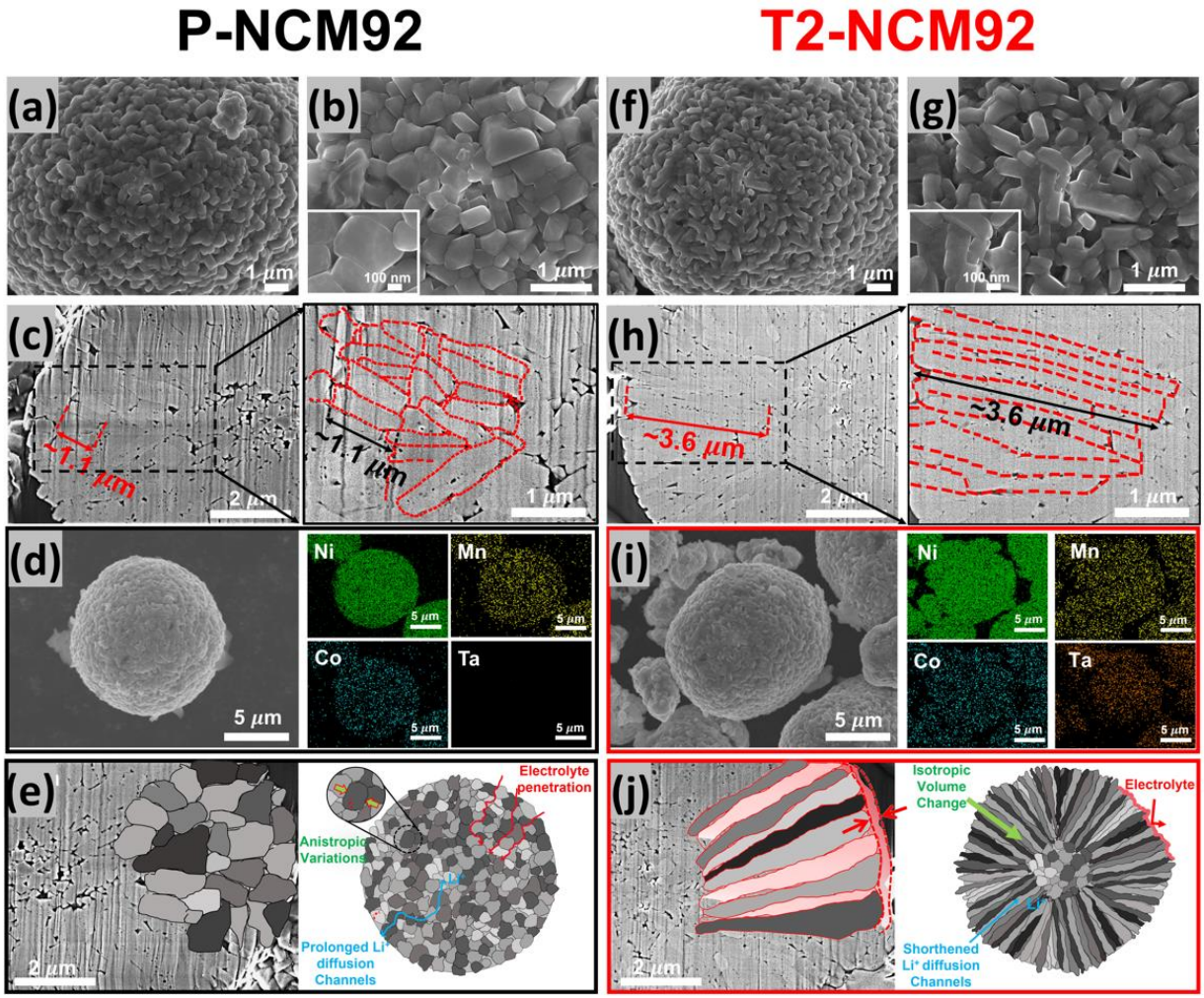

Fig. 2. FE-SEM images of (a) and (b) P-NCM92, (f) and (g) T2-NCM92 samples; FIB-SEM images of (c) P-NCM92, (h) T2-NCM92, the corresponding the energy dispersive X-ray spectroscopy (EDS) elemental mapping of (d) P-NCM92, and (i) T2-NCM92; Schematic images of (e) P-NCM92, and (j) T2-NCM92 structures.

To further investigate the morphological and microstructural changes caused by Ta-modification in the NCM92 cathode active material, field-emission scanning electron microscopy (FE-SEM) and focused ion beam (FIB) analyses of the P-NCM92 and T2-NCM92 samples were performed (Fig. 2). Fig. 2a and f show the microstructure of T2-NCM92, which is more compact than that of P-NCM92. These results are consistent with the Brunauer–Emmett–Teller (BET) surface area study results (Fig. S7 and Table S2), where the average pore diameters determined by the Barrett–Joyner–Halenda (BJH) method for P-NCM92 and T2-NCM92 were approximately 0.534 and 0.438 m^2 g^{-1}, respectively. However, no apparent

differences were observed in the morphologies of the secondary particles. The secondary particles of all NCM92 samples exhibited spherical or quasi-spherical structures with an average diameter of ~14.5 μm. Significant differences were observed in the microstructures and morphologies of the primary particles. Surprisingly, the P-NCM92 particles (Fig. 2b) exhibited short and thick equiaxed primary particles with random orientations, whereas the primary particles of the T2-NCM92 powders (Fig. 2g) were thin, elongated, and tightly packed along the radial directions.

Fig. 2c and h show the FIB-SEM images of P-NCM92 and T2-NCM92 particles, respectively. The Ta-modification of NCM92 material facilitates the formation of elongated grains characterized by thin and extended structures, with lengths reaching ~3.6 μm. These elongated grains exhibited a distinctive radial alignment pattern, extending from the particle center towards the surface, resembling rod-like morphology. By contrast, the grain of the P-NCM92 sample exhibited a dissimilar morphology characterized by short, bulky structures, with a length of ~1.1 μm. These grains display a random orientation throughout the material. Hence, the Ta modification NCM92 sample played a crucial role in the formation of the desired radially aligned, needle-like shape with fine structure within the primary particles. Fig. S8a-c shows the FIB-SEM images of the T10-NCM92 sample. From these studies, incorporating a large amount of Ta leads to the formation of a dense structure with porous and indistinct grain boundaries, which is quite different from T2-NCM92 particles. Those structures are undesirable as they can easily initiate microcracks during the lithiation/delithiation process [41]. It also reduces the lattice spacing between Li layers, which may hinder the transport of Li^+ ions [34,36,41]. Furthermore, Fig. S8d and e (as shown in supporting information) show the EDS linear scanning of the cross section for T10-NCM92. The results prove the presence of Ta^{5+} in the NCM92 structure, which functions as a dopant.

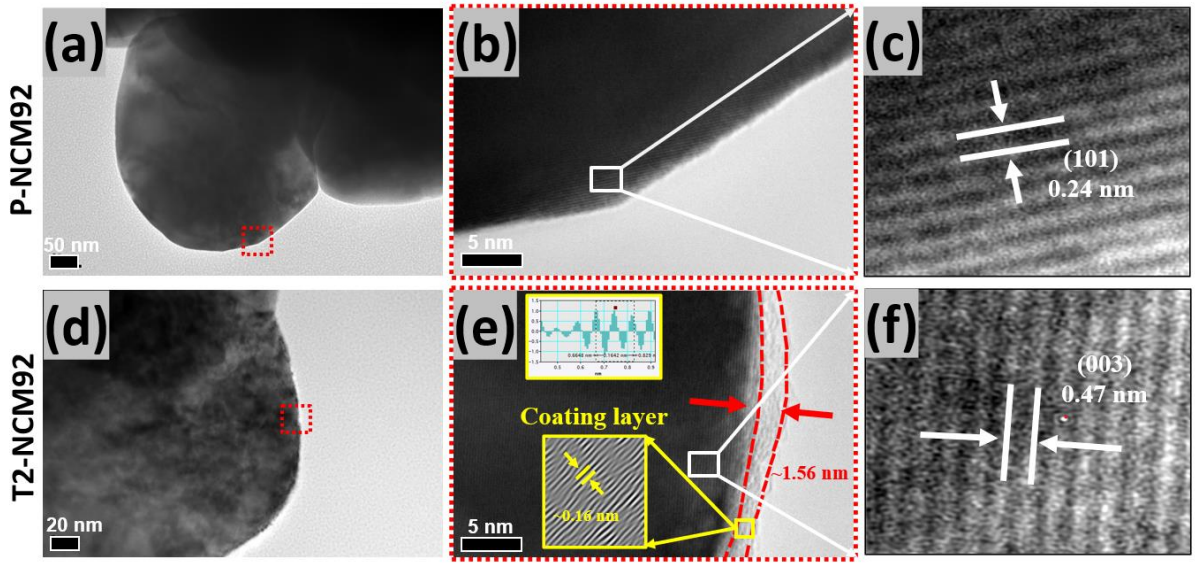

Fig. 3. TEM images of (a–c). P-NCM92, (d–f). T2-NCM92 samples.

The development of a radially aligned microstructure in T2-NCM92 could be interpreted through: (1). surface energy modification of the primary particles, which alters the primary particle shape; and (2). the mechanism of the high-valance (Ta^{+5}) effects on the inhibition of grain coarsening, including the incorporation into bulk and the grain boundary coating. The suitable amount of Ta^{5+} doping, resulting in the modified surface energy of the primary particles [22]. In T2-NCM92 crystals, the (003) and (104) planes are the typical facets found (Fig. 3f). Incorporating 0.2 mol% Ta into NCM92 (i.e., T2-NCM92) selectively reduced the energy of the (003) planes and restrained the fusion and coarsening of the particles, which forced the primary particles to grow in a thin and elongated direction [42,43]. In the case of the as-prepared P-NCM92 sample, the (101) planes were dominant, resulting in thick and nearly equiaxed primary particles [42,43]. In addition, it has been reported that high valance elements such as Ta^{+5} are likely to be insoluble in the crystal structure, resulting in accumulation along the interparticle boundaries. Therefore, the mechanism of doping Ta^{+5} into NCM includes not only incorporation into the bulk, but also grain boundary coating [33,44,45], causing inhibiting boundary migration and retard grain coarsening by segregation of Ta^{+5} at the grain boundary, which can lead to the formation of radially aligned microstructure in T2-NCM92. Moreover,

EDS mapping revealed that Ta was uniformly distributed on the surface of the T2-NCM92 particles (Fig. 2i), indicating that Ta^{5+} partially remained on the particle surface to act as a surface coating and partially diffused into the bulk NCM92 structure to act as a dopant. Unexpectedly, we found that Ta^{5+} performed a dual function, acting as a dopant and surface coating in NCM92. These novel findings imply that the inclusion of Ta in NCM92 provides a dual functional effect that effectively suppresses microcrack formation, accelerates Li^+ ion transport, inhibits electrolyte decomposition, and restrains surface-side reactions. Schematics of the P-NCM92 and T2-NCM92 microstructures are shown in Fig. 2e and j, respectively.

To support the aforementioned findings, high-resolution transmission electron microscopy (HR-TEM), X-ray photoelectron spectroscopy (XPS), and Density functional theory (DFT) simulation studies were performed. HR-TEM images of P-NCM92 and T2-NCM92 samples are shown in Fig. 3. The P-NCM92 and T2-NCM92 particles exhibited a clear interplanar lattice fringe visible along the fine edges (Fig. 3a, b, d, and e). The interplanar crystal spacing of P-NCM92 was *ca*. 0.24 nm (Fig. 3c), matching well with the (101) plane confirmed by the correspondent Fourier transform (FFT) and inverse Fourier transform (IFFT) analysis (Fig. S9). Meanwhile, the T2-NCM92 sample shows the lattice fringe with a *d-spacing* of 0.47 nm that corresponds to the highly crystalline (003) lattice planes (Fig. 3f). In addition, a coating layer was observed on the surface of the T2-NCM92 sample with a layer thickness of approximately 1.5–2 nm (Fig. 3e). The observed coating layer had a lattice spacing of ~0.16 nm, which is likely correlated to the lithium tantalum oxide (Li_7TaO_6) with the (214) plane (Fig. 3e) [46,47]. Therefore, during the synthesis of T2-NCM92, Ta^{5+} diffused into the NCM92 particles along the grain boundaries while excessive Ta^{5+} remained at the surface and reacted with the Li source.

Furthermore, XPS analysis was performed to evaluate the Ta-based surface coating, elemental valence, and surface elemental properties of P-NCM92 and T2-NCM92. The

corresponding spectra were analyzed using the Gaussian-Lorentzian method and given in Fig. 4 and S10. Fig. 4 and S10 show the Ni 2p, Co 2p, Mn 2p, O 1s, Li 1s, and C 1s XPS profiles of P-NCM92 and T2-NCM92, respectively. However, the Ta 4f binding energies were discovered only in T2-NCM92 samples, located at 25.3 and 27.5 eV for Ta $4f_{7/2}$ and Ta $4f_{5/2}$, respectively (Fig. 4d), consistent with Ta^{5+} in Li_7TaO_6 [45,47,48]. Notably, the presence of Li_7TaO_6 on the surface of the T2-NCM92 particles was confirmed, which agrees with the TEM and EDS results. Moreover, according to the C 1s spectrum (Fig. 4c) of both samples, two peaks were observed at 284.6 and 289.9 eV, corresponding to the C−C and CO_3^{2-} peaks, respectively [45,49,50]. Furthermore, in the O 1s spectrum (Fig. 4b), two peaks at 529.3 and 531.7 eV are observed, which are related to the lattice oxygen in a metal framework ($O_{lattice}$) and the $O_{impurity}$ [51]. The $O_{lattice}$ is originated from the lattice oxygen O^{2-} of the M−O (M=Ni, Co, Mn) bond [50], and the $O_{impurity}$ is derived from the active oxygen species O^-,O^{2-}, or CO_3^{2-} impurity layer (e.g., LiOH/Li_2CO_3) on the surface [50]. The area percentage of the $O_{impurity}$ is 72.97% for the P-NCM92 and 48.25% for the T2-NCM92, suggesting that the amount of impurities layer (e.g., Li_2CO_3 and LiOH) on the surface particles are effectively suppressed for T2-NCM92, which is consistent with the C 1s spectrum (e.g., CO_3^{2-} peak) [50,52]. Furthermore, both samples showed binding energies of Ni $2p_{1/2}$ and Ni $2p_{3/2,}$ located at 855 and 872 eV [53], respectively, as shown in Fig. 4a. The Ni $2p_{3/2}$ spectrum involves a mixed valence state corresponding to Ni^{2+} and Ni^{3+} ions, which are located around 854.6 and 856.4 eV [53–55]. The area percentage of the Ni^{3+} peak in P-NCM92 and T2-NCM92 calculated from the Ni $2p_{3/2}$ are 72.41% and 41.12%, respectively. The lower content of Ni^{3+} peak in T2-NCM92 sample, presumably owing to the presence of Ta^{+5} at the TM sites, induced the reduction of the Ni^{3+} into Ni^{2+} to preserve the electroneutrality of the lattice [33,34]. Fig. S10b and c show the Co 2p and Mn 2p peaks of P-NCM92 and T2-NCM92, respectively. Both samples displayed a similar peak of Co $2p_{3/2}$ and Mn $2p_{3/2}$, located at approximately 780.4 and 642.6 eV [52,56,57], respectively, suggesting that the oxidation states of Co and Mn did not change after incorporating Ta into NCM92 bulk

phase. Based on the XPS fitting results, the Co elements in the samples were Co^{3+} and Co^{2+} [52,56,57], whereas Mn was present mainly in the form of Mn^{4+} and Mn^{3+}[52].

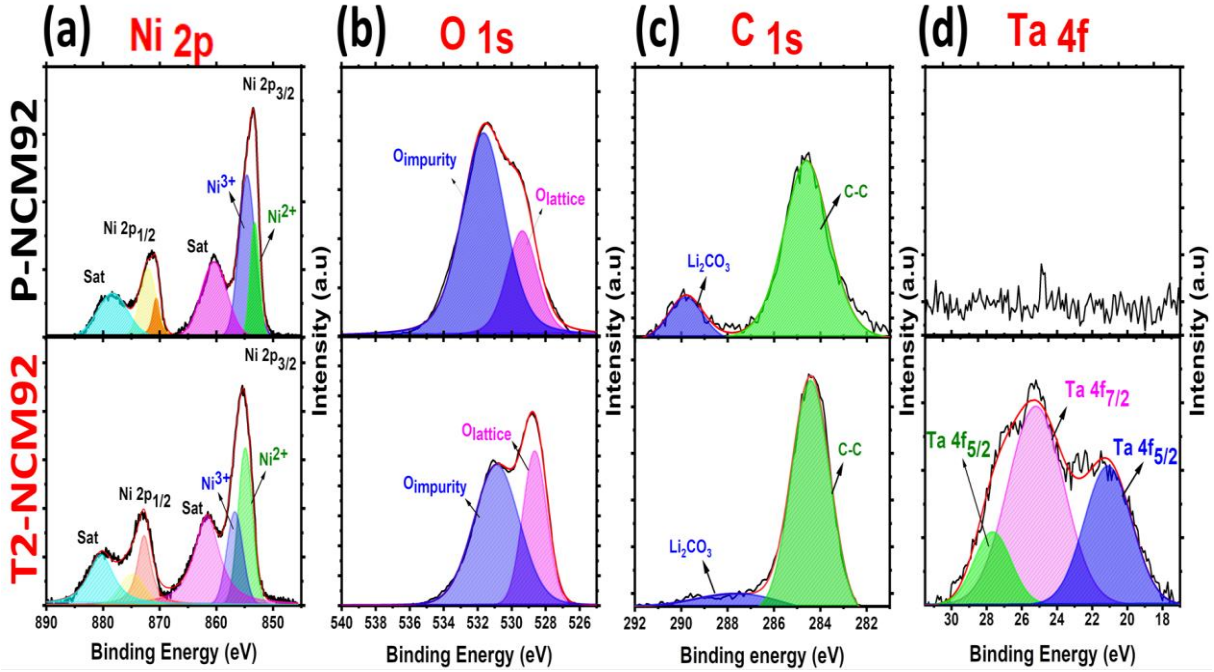

Fig. 4. XPS spectra of P-NCM92 and T2-NCM92 surfaces: (a). Ni 2p, (b). O 1s, (c). C 1s, (d). Ta 4f.

In order to further understand the reason that causes the dual functional effect in T2-NCM92 sample and the influence of excess Li on the formation of a coating layer on the surface of the T2-NCM92 particle, the XRD, FE-SEM, FIB-SEM, and HR-TEM analysis of T2-NCM92 sample with different amounts of excess Li were performed. Fig. S11 shows the XRD patterns of T2-NCM92 oxide powder at Li-excesses of 0, 1, 4, and 8 mol%. All of the samples provided the same characteristic diffraction peaks with no Ta-based compounds detected. However, the Rietveld refinement results revealed that the Li-excess affects the lattice parameter and the cation mixing of the T2-NCM92 sample, as presented in Fig. S12 and Table S3. The lattice parameters (*a* and *c*) and cell volume decreased with increasing Li-excess amount, as shown in Table S3 [34]. The value of Ni^{2+}/Li^{+} in 3b site and the peak intensity $I_{(003)}/I_{(104)}$ ratio indicates the Li/Ni cation mixing [26,53,58]. The ratio of $I_{(003)}/I_{(104)}$ increased upon increasing the excess Li to 4%, and decreased when the excess Li was increased to 8%,

which implies that when the excess Li was higher than 4%, extra Li^+ ions would occupy TM sites, and more Ni^{3+} would be reduced to Ni^{2+} to maintain the charge-balance, which increase the Li/Ni cation mixing [35]. Interestingly, compared to other samples, the T2-NCM92 with 4% Li-excess shows better splitting of the (006)/(102) and (108)/(110) peaks, which indicates a highly ordered layered structure. Furthermore, the crystallite (grain) size of the P-NCM92 and T2-NCM92 samples with different amounts of excess Li was determined using the Scherrer equation [28]. The results showed that excess Li in T2-NCM92 slightly affected the grain size. The grain size of T2-NCM92 oxide powder at Li-excesses of 0, 1, 4, and 8 mol% was *ca.* 34.7, 37.0, 38.3, and 42.0 nm, which is smaller than that of P-NCM92 (*ca.* 49.6 nm), confirmed by FE-SEM results, Fig. S13.

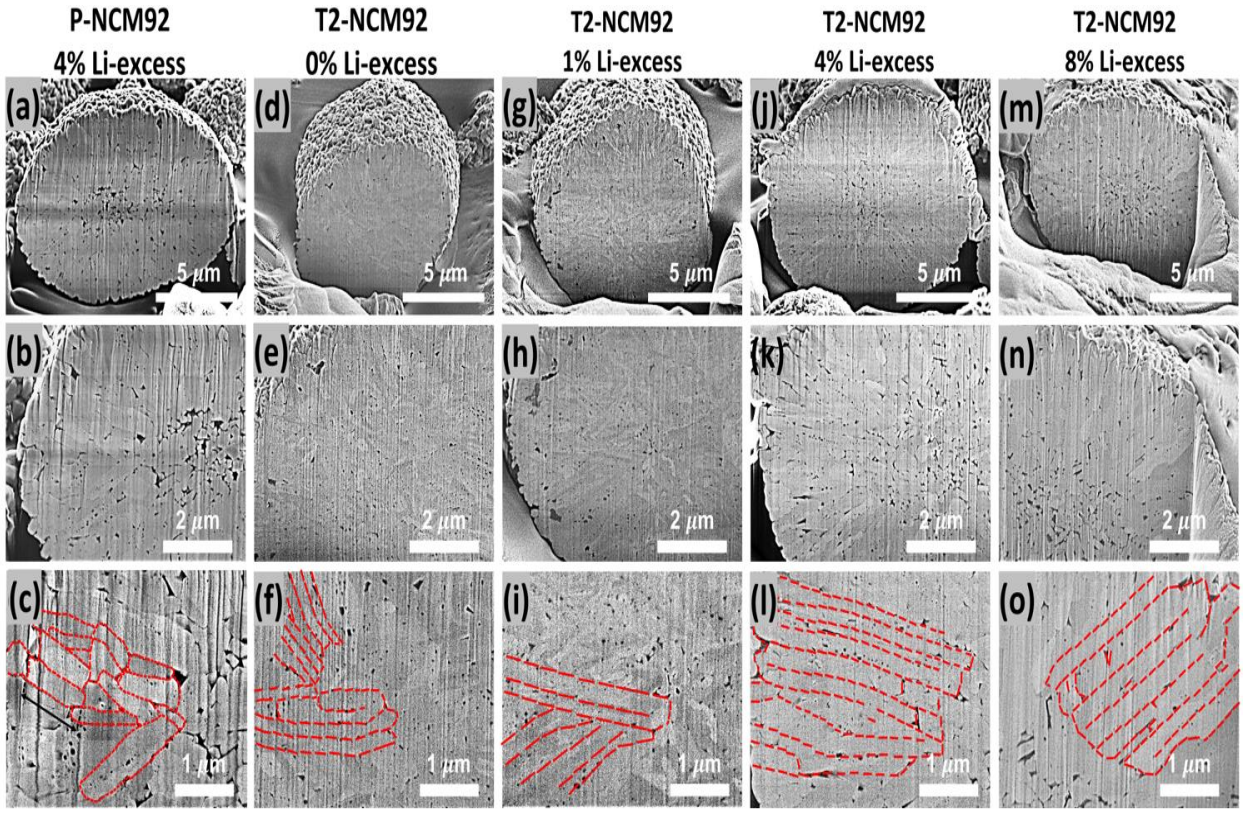

Fig. 5. FIB-SEM images of (a-c). P-NCM92 at 4% Li-excess, and T2-NCM92 powder at different Li-excess, (d-f). 0% Li-excess, (g-i). 1% Li-excess, (j-l). 4% Li-excess, (m-o). 8% Li-excess.

Fig. S13 and Fig. 5 provide the FE-SEM and FIB-SEM images of T2-NCM92 at different excess Li, respectively. Notably, the excess Li slightly affects the grain size (Fig. S13) and subtly alters the microstructure of primary particles (Fig. 5). The primary particle aspect ratios (expressed as length/width) of the P-NCM92 and the T2-NCM92 at Li-excesses of 0, 1, 4, and 8 mol% were approximately between 2 and 7, 4 and 16, 12 and 24, 16 and 25, and 7 and 17, respectively. These results indicate that the T2-NCM92 with 4% Li-excess had narrower aspect ratio distributions. Furthermore, HR-TEM analysis was carried out to understand further the effect of excess Li on the formation of a Li-containing Tantalum oxide (Li_7TaO_6) phase on the surface of the T2-NCM92 particle, as presented in Fig. S14. Fig. S14a and b demonstrate that the coating layer (Li_7TaO_6) was not observed on the surface of T2-NCM92 with 0% and 1% Li-excess. Surprisingly, a Li-containing Tantalum oxide (Li_7TaO_6) phase was observed on the surface of T2-NCM92 when the amounts of excess Li were 4 and 8%, with the thickness of 1.56 and 6.02 nm, respectively (Fig. S14c and d). These results demonstrated that the suitable extent of Li-excess can compensate for the Li loss during calcination and react with excessive Ta^{5+} to form Li_7TaO_6 phase on the surface NCM92 particles. It is also imperative to note that increasing Li-excess to 8% will develop an excessively thick Li_7TaO_6 surface layer with relatively low electronic conductivity. Therefore, a suitable amount of Ta and excess Li is needed to form a thin conductive protective coating layer (Li_7TaO_6) and microstructure modification on NCM92.

3.3. Mechanism of incorporation of Ta into NCM92

DFT calculations were performed to study whether Ta^{5+} acted as a dopant and/or surface-modifying agent in NCM92. To simplify our simulation, the $LiNiO_2$ (LNO) structures with 1% and 2% Ta were modeled [29–32]. To maintain charge neutrality in Ta-modified LNO (T-LNO) and the formation of a Li-containing Tantalum oxide (Li_7TaO_6) phase after the interaction of Ta_2O_5 with LNO in the presence of oxygen, as shown in Table 1, Li vacancies

were introduced into T-LNO. The inclusion of the Li_7TaO_6 structure in the reaction was motivated by the observation of a thin surface layer on the T2-NCM92 sample in the HR-TEM image, which showed a lattice spacing of approximately 0.16 nm (Fig. 3e).

Table 1 Model simulation result for Ta incorporation into LNO and their corresponding energies

	Chemical reactions		Energy (eV)
(i)	$0.99LiNiO_2 + 0.009Ta_2O_5 + 0.014O_2$	$\rightarrow Li_{0.93}Ni_{0.99}Ta_{0.009}O_2 + 0.009Li_7TaO_6$	−0.034
(ii)	$0.98LiNiO_2 + 0.014Ta_2O_5 + 0.012O_2$	$\rightarrow Li_{0.92}Ni_{0.98}Ta_{0.019}O_2 + 0.009Li_7TaO_6$	−0.041

The calculated reaction energies were negative, indicating that Ta^{5+} could be incorporated into the Ni-rich system to form a Ta-containing surface coating with a Li_7TaO_6-based structure. The Ta^{5+}-doped models, namely $Li_{0.93}Ni_{0.99}Ta_{0.009}O_2$ and $Li_{0.92}Ni_{0.98}Ta_{0.019}O_2$ showed a slight increase in the lattice parameters *a* and *c*, which is also in agreement with the experimental lattice parameters, as shown in Tables S1 and S4. The interlayer and intralayer distances are shown in Fig. S15. The change in the interlayer distance was due to Li vacancies. However, the addition of Ta to the Ni-rich systems did not significantly change the intralayer distance. These simulated results suggest that Li vacancies, which form because of the high oxidation state of Ta^{5+} and the formation of Li_7TaO_6 lead to an increase in the lattice volume, as also observed in the experimental analysis, as shown in Table S1.

Furthermore, the presence of Li_7TaO_6 in the reaction implies the formation of an additional surface layer. Based on a previously reported work, the Li_7TaO_6 layer possesses a high ionic conductivity (*ca.* 5.7×10^{-4} S cm^{-1} at 300 K), thereby considerably enhancing interfacial Li^+-ion transport [59]. Moreover, this surface layer can protect the Ni-rich cathode material against electrolyte HF attack, suppress interfacial secondary reactions, and reduce interfacial impedance growth. Thus, it can improve the electrochemical and long-term cycling stability. However, notably, an excessively thick Li_7TaO_6 surface layer with relatively low

electronic conductivity may result in increased resistance [59]. As illustrated in Fig. 10, Table S7 and S8, the impedance of T3-NCM92 was higher than those of T1- and T2-NCM92. Therefore, optimizing the thickness of the Ta-based surface coating layer is important for enhancing the electrochemical stability of Ni-rich systems. Notably, the primary particles of T2-NCM92 were needle-like, probably due to the surface energy modification effect, where the (003) surface of T2-NCM92 is more favorable than the (104) surface. Thus, the granular shape of the primary particles in pristine Ni-rich NCM92 changed to a needle-like shape after Ta doping. This finding aligns with the microstructures observed in our previous simulation studies on Ni-rich cathode active materials [60]. However, no Li_7TaO_6 surface layer was observed. This difference can be attributed to the synthesis procedure, particularly the variations in the mixing step involving the Ta_2O_5 precursor and the amount of excess Li. Importantly, in the current work, T2-NCM92 exhibited doping in the bulk and surface coating of the primary particles, as well as in the secondary particles, which can markedly alter the microstructure, morphology, and particle size of NCM92 after Ta doping. Thus, the incorporation of Ta into our Ni-rich cathode material acted as a doping and coating material, resulting in superior electrochemical properties and long-term cycling stability.

To further investigate the impact of Ta on primary particles, two possible grain boundaries (GBs), namely GB1 ($\Sigma2[\bar{1}\bar{1}20]/(1\bar{1}0\bar{4})$) and GB2 ($\Sigma3[110]/(1\bar{1}02)$) were modeled. These GBs were chosen for their dissimilar atomistic structures, which can result in varied stabilities, Ta segregation, and ionic conductivity. Previous *Ab* initio molecular dynamics simulations conducted by He *et al.* on a Ni-rich NCM showed that Li^+ ion diffusivity (D_{Li^+}) in GB1 is around 10^{-9} $cm^2\ s^{-1}$, higher than that in GB2 [61]. The significantly lower D_{Li^+} in GB2 is attributed to grain shifting along the *z* direction to minimize energy. Our DFT simulations indicate that GB2 is 0.166 eV more favorable than GB1 for T2-LNO, where the Li layer comes into contact with the Ni layer within GB2. This could lead to the obstruction of the Li^+ ion diffusion pathway.

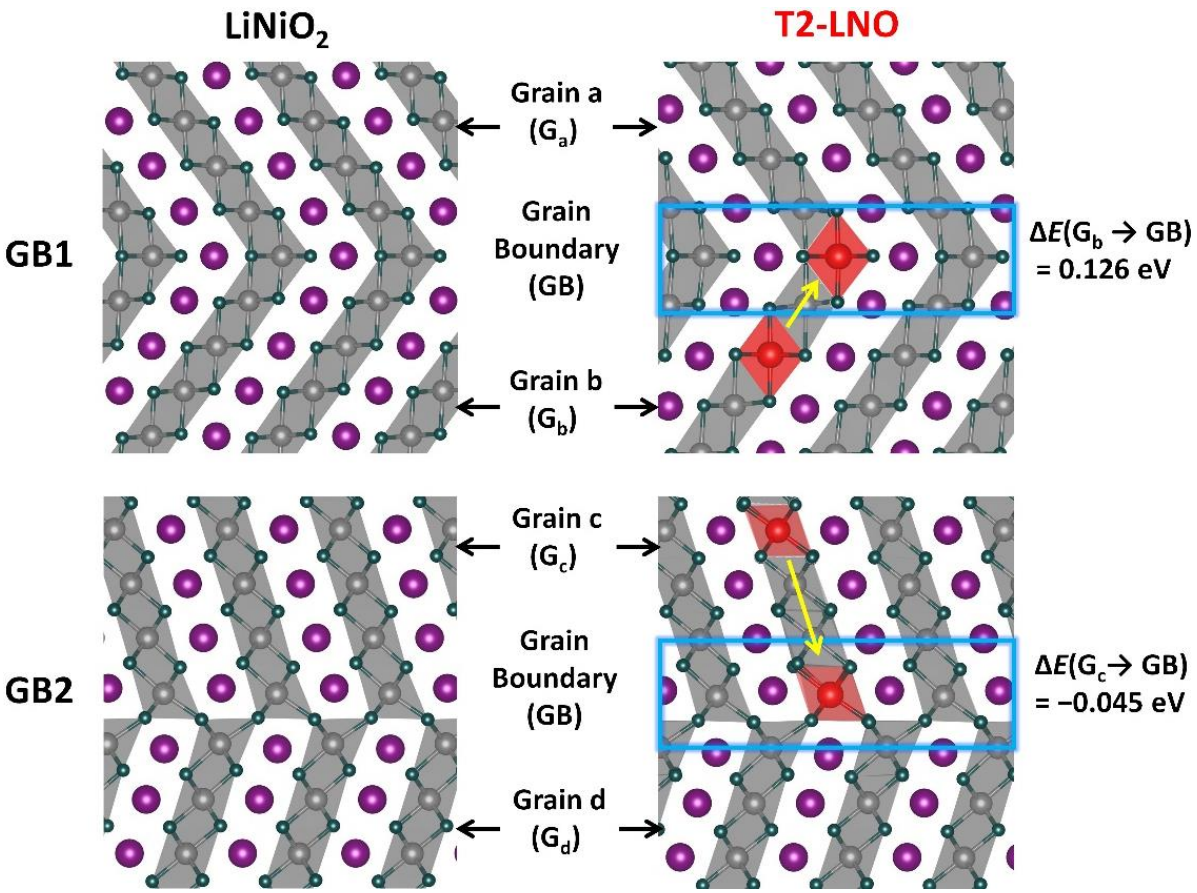

Fig. 6. Side views of GB1 ($\Sigma2[\bar{1}\bar{1}20]/(1\bar{1}0\bar{4})$) and GB2 ($\Sigma3[110]/(1\bar{1}02)$) of $LiNiO_2$ and Ta-modified $LiNiO_2$.

Fig. 6 presents GB1 and GB2 of pristine and Ta-modified LNO. The results reveal that Ta exhibits a preference for remaining in the bulk (ΔE = 0.126 eV) at GB1, while it tends to segregate within the GB (ΔE = −0.045 eV) at GB2. This suggests that Ta modification may tend to stay at GB within GB2 in Ta-modified Ni-rich materials, minimizing their energy. Recent studies have also addressed this observation, highlighting that high charge-state cation modifications (such as W^{6+}) in Ni-rich materials tend to localize at GB rather than substituting Ni or Li sites [62–64]. To gain insight into the reason for Ta segregation at GB within GB2, the lattice parameters *a* and *c* were calculated (Table S5). It was found that the bulk shows larger changes in lattice parameters *a* and *c* compared to those at GB within GB2. Specifically, a −0.54% shrinkage and +0.09% expansion of *a* were found in the bulk and at GB, when Ta was modified at GB2. Moreover, +0.32% and +0.17% increase in *c* were calculated for Ta in the

bulk and at GB within GB2. The results indicate that lattice stress plays a significant role in influencing the modification of Ta.

It is important to highlight that in the present work, T2-NCM92 exhibits doping in the bulk and the surface coating of the primary particles, as well as in the secondary particles, that can alter the microstructure, morphology, and particle size of NCM92 after Ta doping. The schematic representation of the synthesis process for Ta-modified NCM92 secondary particles is depicted in Fig. 7. It is noted that the hydroxide precursor employed in this work is synthesized in a needle-like shape. Without Ta, the secondary particles exhibit granular morphology, while those with Ta doping maintain the needle-like shape. Thus, the incorporation of Ta into our Ni-rich cathode active material acts as doping and coating, resulting in greatly enhanced electrochemical properties and long-term cycling stability.

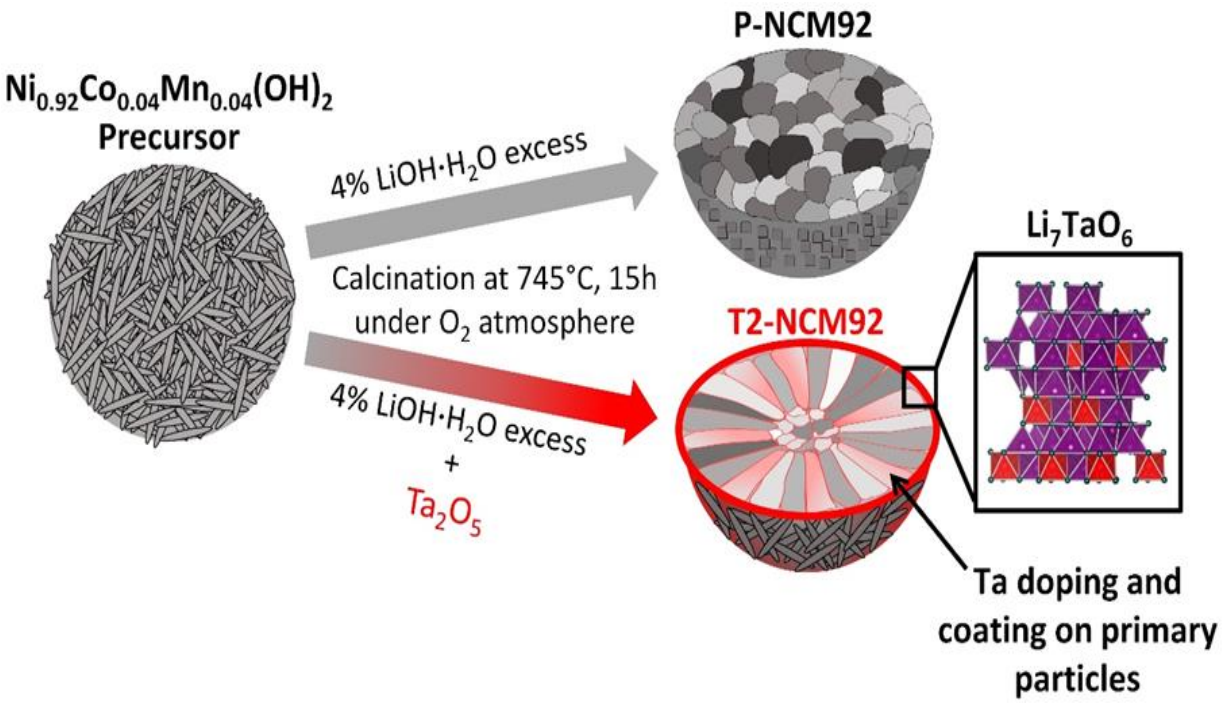

Fig. 7. Schematic illustration of the synthesis process for P-NCM92 and T2-NCM92.

3.4. Structural analysis of Ta-modified NCM92

To evaluate the electrochemical performance of P-NCM92 and Tx-NCM92 as cathode active materials in LIB, a 2032 coin-type half-cell with a Li metal anode was assembled and evaluated (Fig. 8). The initial charge-discharge profiles for all the P-NCM92 and Tx-NCM92-based cathodes were tested at the C-rates of 0.1C (1C = 200 mA g^{-1}) within the range of 2.8–4.3 V at 30 °C, as shown in Fig. 8a. All samples exhibited comparable charge/discharge voltage profiles, implying that P-NCM92 and Tx-NCM92 exhibited comparable electrochemical properties. However, the initial discharge capacity of the Tx-NCM92 cathode was slightly lower than that of P-NCM92 (Fig. 8a), which was related to the electrochemical inactivity of Ta^{5+}. In the lattice sites, Ta^{5+} replaces Ni^{3+}, thereby reducing the total number of active TM cations [65].

Fig. 8b displays the high-rate discharge capability test for P-NCM92 and Tx-NCM92 cathodes with continuous cycling at incremental rates from 0.2C to 10C, and adjacent reversals to 0.2C. No significant differences in discharge capacities between P-NCM92 and Tx-NCM92 cathodes at C-rates of 0.2C, 0.5C, 1C, 5C, and 10C are observed. However, after decreasing the C-rate again, the obtainable specific capacity of Tx-NCM92 is significantly higher than that of P-NCM92. The discharge capacity of P-NCM92 and T2-NCM92 cathodes after the rates returned to 0.2C is *ca.* 189.5 mAh g^{-1} (the capacity recovery capability of 94.1%) and 197.8 mAh g^{-1} (the capacity recovery capability of 98.7%), respectively. Notably, incorporating Ta into the NCM92 structure offers excellent electrochemical reversibility and enhances the capacity recovery performance owing to the Ta^{5+} occupying the TM (Ni^{3+}) site. These Ta^{5+} expand the diffusion pathway and accelerate the Li^{+} ion transport within the lattice, which is in agreement with our Rietveld refinement result [65]. Therefore, the benefits of Ta modifications of NCM92 are reflected in its long-term cycling stability performance.

Fig. 8c shows the cycling stability test results performed at 30 °C at C-rates of 1C within 2.8–4.3 V. After 100 cycles, the P-NCM92, T1-NCM92 (0.1 mol% Ta), T2-NCM92 (0.2 mol% Ta), and T3-NCM92 (0.3 mol% Ta) cathodes provided the discharge capacity retentions of 70.5%, 88.5%, 95.7%, and 90.8%, respectively, with average coulombic efficiency of 99.2%, 99.2%, 99.6%, and 99.1%. These results proved that incorporating Ta into the NCM92 sample significantly enhanced the electrochemical performance, particularly the long-term cycling stability.

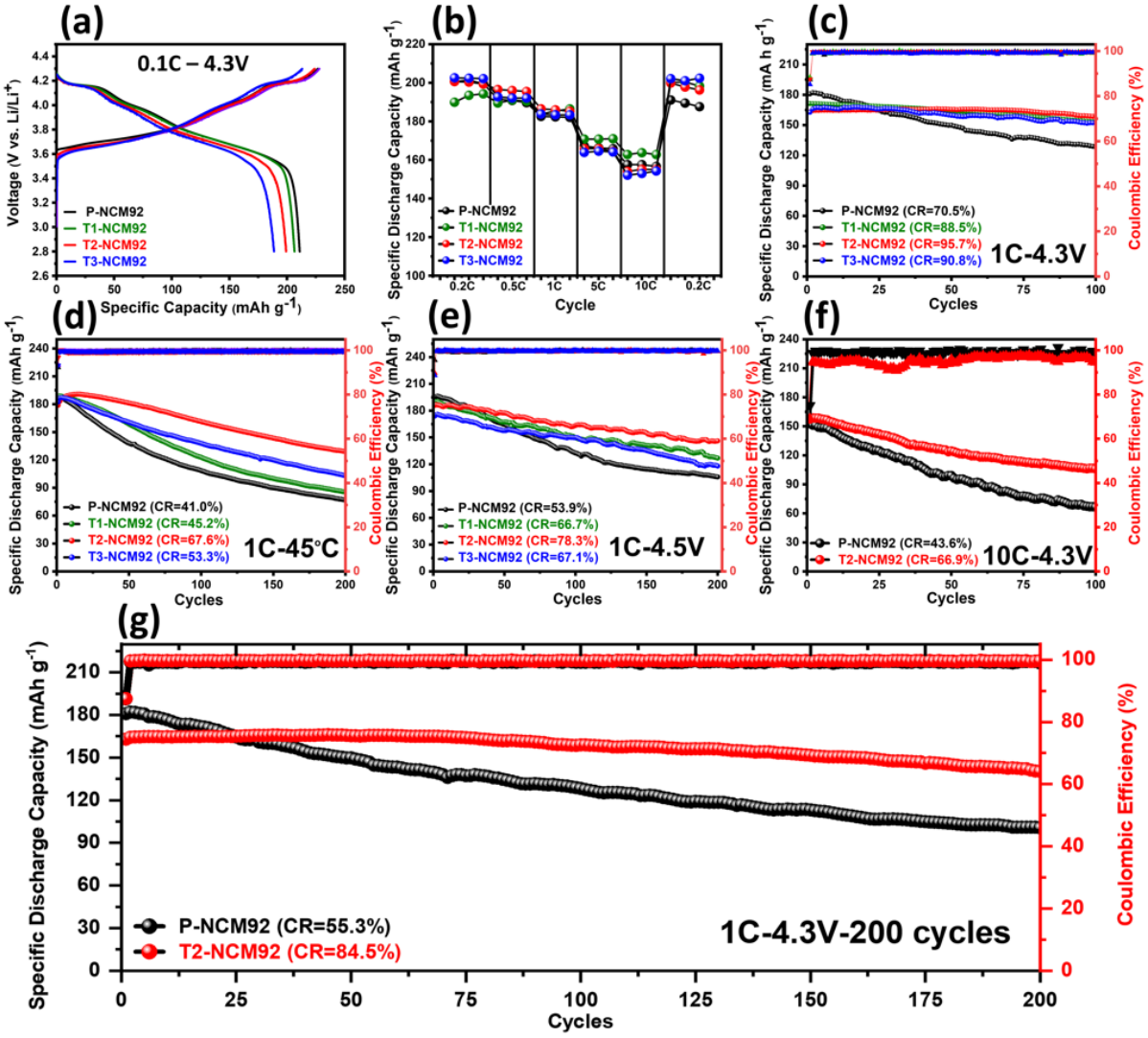

Fig. 8. (a). Initial charge/discharge profiles at 0.1C (1C = 200 mA g^{-1}), (b). Rate capabilities performance. Cycles performance at the C-rates of 1C, (c). at 4.3 V for 100 cycles, (d). 45℃ for 200 cycles, and (e). 4.5 V for 200 cycles, (f). Cycling performance at the high C-rates of 10

C for 100 cycles at 4.3 V, (g). Long-term cycling performance at the C-rates of 1C at 4.3 V for 200 cycles.

The long-term cycling stabilities of P-NCM92 and Tx-NCM92 electrodes were tested under various conditions. These conditions included elevated temperature (45 °C), high-working voltage (up to 4.5 V (*vs.* Li/Li^+)), high C-rates (up to 10C), and extensive cycling (up to 200 cycles), as shown in Fig. 7d-g. The aforementioned harsh and relevant parameters were selected to strain NCM92 and evaluate its structural and electrochemical stability for any real-world application. Fig. 8d shows the cycling performance of P-NCM92 and Tx-NCM92 cathodes measured at an elevated temperature of 45 °C at 1C/1C (charge/discharge rate) in the voltage range of 2.8–4.3 V. The T2-NCM92 cathode exhibited superior discharge capacity retention, with a value of 67.6% after 200 cycles. In comparison, the capacity retentions of the P-NCM92, T1-NCM92, and T3-NCM92 cathodes were approximately 41.0%, 45.2%, and 53.3%, respectively, over the same cycling period. Moreover, Fig. 8e shows the cycling performance at higher upper voltages of 4.5 V (cycling between 2.8–4.5 V) at 1C/1C over 200 cycles at 25 °C. The T2-NCM92 cathode exhibited a capacity retention of 78.3%, while the P-NCM92, T1-NCM92, and T3-NCM92 cathodes provided a capacity retention of only 53.9%, 66.7%, and 67.1%, respectively.

The high C-rate performance at 10C of the P-NCM92 and T2-NCM92 cathodes is illustrated in Fig. 8f (2.8–4.3 V at 30 °C). Cycling at 10C leads to the rapid degradation of the electrochemical performance of P-NCM92 and after 100 cycles only 43.6% of its initial discharge capacity (initial specific discharge capacity of 152.6 mAh g^{-1}) was useable. T2-NCM92 electrode showed significantly better capacity retention of 66.9% at 10 C after 100 cycles, with an initial discharge capacity of 157.6 mAh g^{-1}. However, the Coulombic efficiency of T2-NCM92 at a high rate (10C) performance fluctuates compared to P-NCM92 (Fig. 8f). This fluctuation might occur due to when 0.2% mol Ta incorporated into NCM92 (denoted as T2-NCM92), it will improve the ionic conductivity, as shown in GITT measurement (Fig. 10a

and b). However, electronic conductivity is not improved by the same trend, as presented in Fig S16. In addition, Fig. 8g shows the long-term cycling stability of P-NCM92 and T2-NCM92 cathodes over 200 cycles at the current rate of 1C within 2.8–4.3 V at 30 °C. The P-NCM92 cathode exhibited an inferior capacity retention of only 55.3% after 200 cycles. By contrast, the T2-NCM92 cathode exhibited stable cyclability, with a capacity retention of 84.5% after 200 cycles. Thus, Ta modification of NCM92 is beneficial for structural stability and electrochemical performance improvement even under harsh conditions, such as at elevated temperature (45 °C), high-working voltage (up to 4.5 V (*vs*. Li/Li^+)), high C-rates (up to 10C), and extensive cycling (up to 200 cycles).

A comparison of the T2-NCM92 sample with other reported highly Ni-rich NCMs samples and their modifications (e.g., doping or coating) is shown in Table 2. Notably, the presented T2-NCM92 (0.2 mol% Ta) cathode shows better electrochemical performance than the previously reported Ta-modified NCMs [24,26,73,58,66–72]. The improvement in the electrochemical performance after Ta modification of NCM92 is attributed to the high BDEO (*ca.* 839 kJ mol^{-1}) value of Ta^{+5}, which leads to increased TM−O bond energy and activation energy for the extraction of oxygen from the NCM92 structure, thereby suppressing surface phase transformation and structural degradation and improving cycling stability even at a high delithiation level and temperature [19,25,74–76]. Nevertheless, T1-NCM92 and T3-NCM92 cathodes exhibit inferior performance than T2-NCM92 one, owing to the inhomogeneous Ta modification resulting in agglomeration, as confirmed by SEM-EDS (Fig. S6). The superior performance of the T2-NCM92 cathode compared to the other Tx-NCM92 samples is closely related to the integrated and synergistic effect (i.e., bifunctional effect-doping and coating at one time) of the Ta-enriched phase on the surface and thin, elongated, and tightly packed primary particles along the radial directions, as demonstrated in the FE-SEM, FIB-SEM, EDS, TEM, HR-TEM, and XPS analyses.

Table 2 Comparison of the electrochemical performance of the previously reported modified Ni-rich NCM cathode active materials based on coating and doping strategies

Sample	Strategies	Voltage (V)	Current	Capacity Retention	Rate	Capacities	Ref.
$LiNi_{0.92}Co_{0.04}Mn_{0.04}O_2$	Si-doping	2.5–4.4 V	0.3C	75.2%@100th	2C	149.5 mAh g^{-1}	[24]
$LiNi_{0.92}Co_{0.04}Mn_{0.04}O_2$	Zr-doping	2.5–4.4 V	0.3C	83%@100th	2C	162.2 mAh g^{-1}	[66]
$LiNi_{0.90}Co_{0.05}Mn_{0.05}O_2$	Lithium tungsten Oxide-coating	3.0–4.3 V	0.5C	84.6%@80th	5C	~60 mAh g^{-1}	[58]
$LiNi_{0.92}Co_{0.05}Mn_{0.03}O_2$	Ti and B-doped	2.7–4.3 V	1C	78.3%@100th	5C	160 mAh g^{-1}	[67]
$LiNi_{0.92}Co_{0.06}Al_{0.02}O_2$	W^{3+} cation and BO_3^{3-} polyanion co-doping	2.8–4.3 V	1C	93.4%@100th	10C	155.3 mAh g^{-1}	[68]
$LiNi_{0.90}Co_{0.05}Mn_{0.05}O_2$	Sn-doped	2.8–4.3 V	1C	92.2%@100th	-	-	[23]
$LiNi_{0.9}Co_{0.05}Mn_{0.05}O_2$	Ce-doped	2.7–4.3 V	0.5C	80.5%@100th	-	-	[69]
$LiNi_{0.90}Co_{0.04}Mn_{0.03}Al_{0.03}O_2$	Al-doping and Li_2ZrO_3 coating	2.8–4.3 V	1C	90.2%@100th	10C	151 mAh g^{-1}	[70]
$LiNi_{0.9}Co_{0.04}Mn_{0.03}Al_{0.03}O_2$	Li_3VO_4-coating	3.0–4.3 V	1C	90.5%@100th	5C	162.2 mAh g^{-1}	[71]
$LiNi_{0.90}Co_{0.05}Mn_{0.05}O_2$	Li_2SiO_3-coating	2.7–4.3 V	2C	88.2%@100th	5C	147.5 mAh g^{-1}	[73]
$LiNi_{0.94}Co_{0.04}Al_{0.02}O_2$	Ta-doping	2.8–4.3 V	0.5C	93.6%@100th	5C	158.5 mAh g^{-1}	[65]
$LiNi_{0.92}Co_{0.04}Mn_{0.04}O_2$	**Ta-surface coating and doping**	**2.8–4.3 V**	**1C**	**84.5%@200th**	**10C**	**157.6 mAh g^{-1}**	**This work**

3.5. Electrochemical Kinetic of Ta-modified NCM92

To study the structural variations in the cathodes during the cycling, the differential capacity curves (dQ/dV) were performed at 1C by charging to 4.3 V within 100 cycles. Fig.

S17a-d demonstrate the presence of three redox peaks related to the multifarious phase changes that occur during lithiation/delithiation. In comparison with the Tx-NCM92 cathodes, the intensities of the H2–H3 cathodic peaks of the P-NCM92 cathode were significantly reduced upon successive cycling, as shown in Fig. S17a, suggesting a significant impact on the H2–H3 phase transition in the P-NCM92 cathode [54,77]. The H2–H3 phase transition region is most likely owing to the continuous rapid unit cell volume change, which causes stress and strain generation because of the lattice mismatch, resulting in fast capacity fading [77]. Notably, the redox peaks shift during cycling, indicating cathode polarization [54,58,76]. For the P-NCM92 sample (Fig. S17a), the typical cathodic peak continuously shifted to a lower potential with increasing cycle number, demonstrating severe polarization, fast electrochemical degradation, and impedance growth [76,78]. However, after Ta^{5+} doping into the NCM92 structure (Figure S17b-d), the redox peak position did not significantly shift with electrochemical cycles, which indicates that the lower polarization and H2–H3 phase transition, and OER were effectively suppressed [7,9].

Fig. S17e-h present the cyclic voltammetry (CV) curves of the P-NCM92 and Tx-NCM92-based cathodes. P-NCM92 and Tx-NCM92 show a similar peak trend. All peaks consist of three pairs of redox peaks (i.e., H1–M, M–H2, H2–H3), which reveals that the Ta doping of the NCM92 structure did not change the redox reaction during the intercalation/deintercalation process [54]. In addition, the potential difference (ΔV) of the redox peak provides information regarding the electrochemical reversibility of the cathode and degree of polarization [79]. The potential difference (ΔV) values of P-NCM92, T1-NCM92, T2-NCM92, and T3-NCM92 cathodes were approximately 172.2, 169.4, 165.4, and 165.7 mV, respectively. Our T2-NCM92 electrode showed the lowest potential difference value, indicating the lowest polarization [58,80], which is in good agreement with the dQ/dV result. The appropriate amount of Ta^{5+} incorporation into the NCM92 structure will result in the best electrochemical reversibility and performance. This is due to the suppressed H2–H3 phase

transition, which inhibits the polarization of cathodes and eventually provides remarkable long-term charge/discharge cycling stability, even at harsh conditions, as proven in the charge/discharge test (Fig. 8).

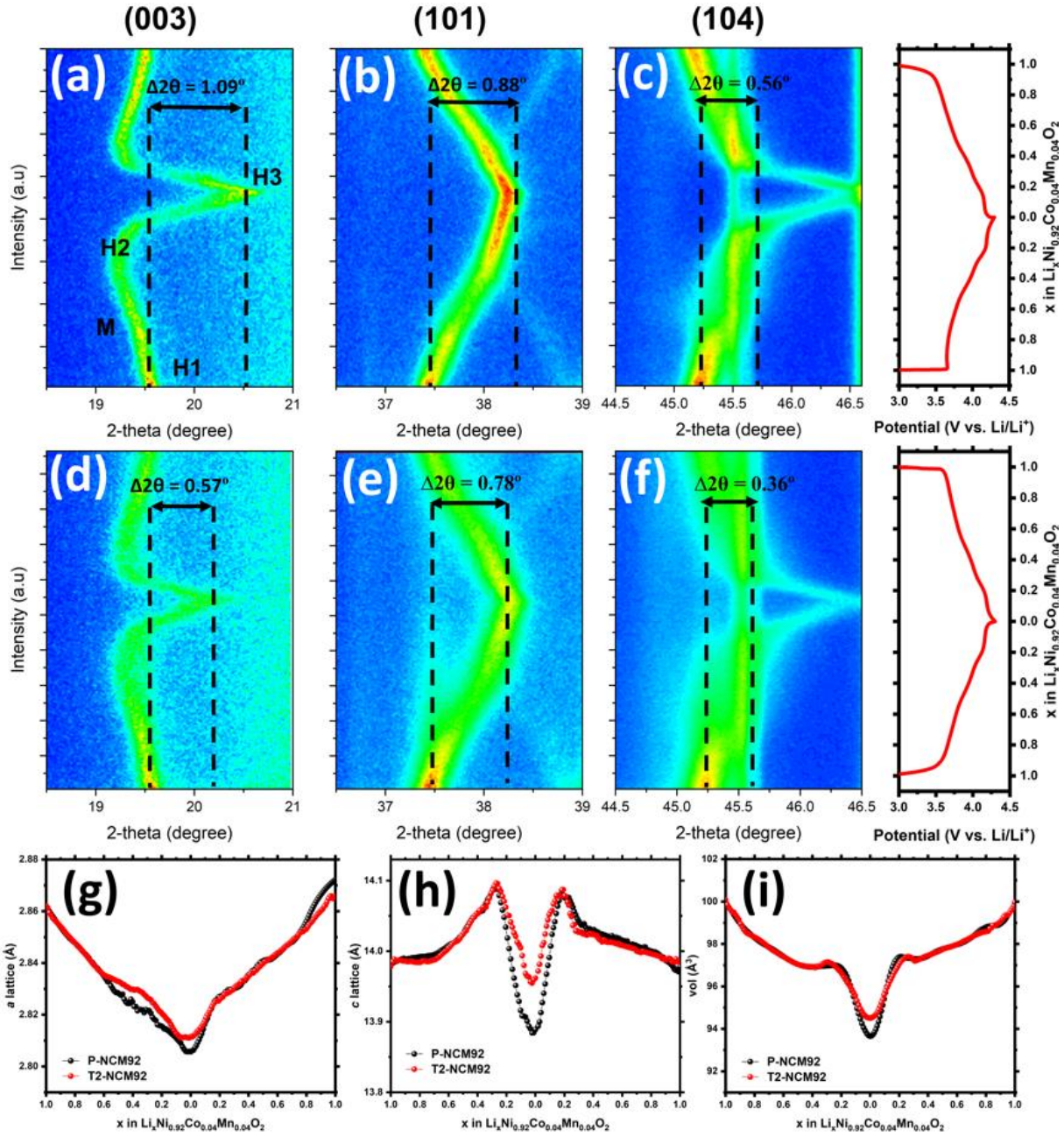

Fig. 9. Contour plots of the intensity at selected 2θ regions from in-situ XRD data recorded on (a–c). P-NCM92, (d–f). T2-NCM92 samples with the cell potential are given at the right of the figure, (g–i). The variation in *a*-axis lattice, *c*-axis lattice, and unit cell volumes as a function of the cut-off voltages.

Furthermore, in-situ XRD experiments were performed to better understand the lithiation and delithiation mechanisms and the structural evolution of the P-NCM92 and T2-NCM92 electrodes. Notably, the shifting of the (003) peaks corresponds to the variation of the *c*-axis, while the (101) peak shift represents the contractions of *a*-plane owing to the reduced TM ionic radius [42]. Fig. 9 shows the shift of the (003) peak to lower angles and the (101) and (104) peaks to higher angles in both samples during charging, accompanied by a gentle phase transition from H1 to H2 to H3.

However, during the discharge process, the trend of the aforementioned peaks exhibited a reverse tendency. Compared to the T2-NCM92 electrode, a significant peak shift was observed in the P-NCM92 electrode, as shown in Fig. 9a, b, and c, indicating severe phase transition and anisotropic lattice distortion within the P-NCM92 cathode [34,70]. In the case of T2-NCM92, the shift of the peaks was lower and steadier (Fig. 9d, e, and f), which suggests that the Li^+ intercalation/deintercalation of T2-NCM92 was more reversible than that of P-NCM92 [34,70,81]. This facilitated smooth phase transitions, alleviated the anisotropic lattice distortion, and enhanced the phase transition reversibility [40,70], thus helping to explain the higher cycling stability in comparison to P-NCM92 (Fig. 8).

The variations in *a*-axis lattice, *c*-axis lattice, and unit cell volumes (V) as a function of the cutoff voltages are shown in Fig. 9g-i, and the Rietveld refinement results with normalized variations of the largest lattice parameters are provided in Table S6. Significant differences were observed in the lattice parameters and unit cell volume between the two samples. A comparative analysis showed that the *a*, *c*, and V parameters of P-NCM92 decreased by 1.96, 1.41, and 6%, respectively, in the initial fully charged state. In comparison, *a*, *c*, and V parameters in T2-NCM92 decreased by 1.77, 0.94, and 5.57%, respectively. These results prove that T2-NCM92 is more electrochemically stable than P-NCM92, which agrees with the dQ/dV and CV results (Fig. S16). Notably, the abrupt anisotropic volume change in the P-NCM92

cathode may have formed numerous microcracks on the particles, leading to severe capacity fading, as shown in Fig. 8.

To further explore the Li^+-ion diffusion coefficients and electrochemical kinetic reversibility inside the P-NCM92 and Tx-NCM92 materials, the galvanostatic intermittent titration technique (GITT) was adopted. Fig. 10a shows the transient voltage curves of the P-NCM92 and T2-NCM92 electrodes, with the selected points (i) and (ii) of the charging and discharging plateaus, confirming that the transient voltage originated from the redox pairs of Ni^{2+} and Ni^{3+}, respectively. Furthermore, the Li^+-ion diffusion coefficients (D_{Li^+}) in the cathodes were calculated as a function of voltages, according to Fick's second law equations with relevant assumptions and simplifications (Fig. 10b) [34,35,82]. The results demonstrated that the Li^+-ion diffusion coefficients (D_{Li^+}) in the T2-NCM92 electrode (1.55×10^{-10}–2.96×10^{-9} $cm^2\ s^{-1}$) are higher than that for the P-NCM92 electrode (1.57×10^{-12}–2.35×10^{-9} $cm^2\ s^{-1}$), which is particularly evident at cell voltages above 3.7 V (*vs*. Li/Li^+). The larger D_{Li^+} value for T2-NCM92 might be attributed to the synergistic effect of the Ta-enriched phase on the surface and radially aligned needle-like morphology of the primary particles (Fig. 2 and 3). The Ta-enriched layer on the surface of T2-NCM92 exhibits good ionic conductivity, which facilitates the promotion of interfacial Li^+-ion transport, and the strong Ta−O bond strength in the structure alleviates the anisotropic lattice structure distortion and maintains larger space channels for Li^+ ion diffusion. In addition, the radially aligned needle-like shapes of primary particles reduce the diffusion path length of Li^+ ions and offer preferable charge distribution upon cycling. The improved Li^+-ion diffusion in the T2-NCM92 electrode is responsible for good high-rate performance, as seen in Fig. 8b and f.

Electrochemical impedance spectroscopy (EIS) was performed to further investigate the effects of the Ta modifications in NCM92 on the electrochemical kinetics and interfacial impedance. Fig. 10c and d show the AC impedance spectra and equivalent circuit model of the NCM92 samples before the cycle and after 200 cycles (at the C-rates of 1C in the voltage range

of 2.8–4.3 V at 30 °C), respectively. Notably, the semicircle in the high-to-low-frequency region arises from the electrode/electrolyte interface and refers to the charge transfer resistance (R_{ct}), where the R_{ct} value predominantly controls the electrochemical reaction [34]. Table S7 and S8 provide AC impedance spectra fitting results for P-NCM92 and Tx-NCM92 electrodes. The results illustrate that the charge transfer resistance values of the T2-NCM92 electrode before the cycle and after 200 cycles are significantly lower than that of P-NCM92. This which implies the internal impedance increase after the intercalation/deintercalation process was significantly suppressed and the electrolyte penetration along the grain boundaries was considerably reduced by Ta doping into the NCM92 structure.

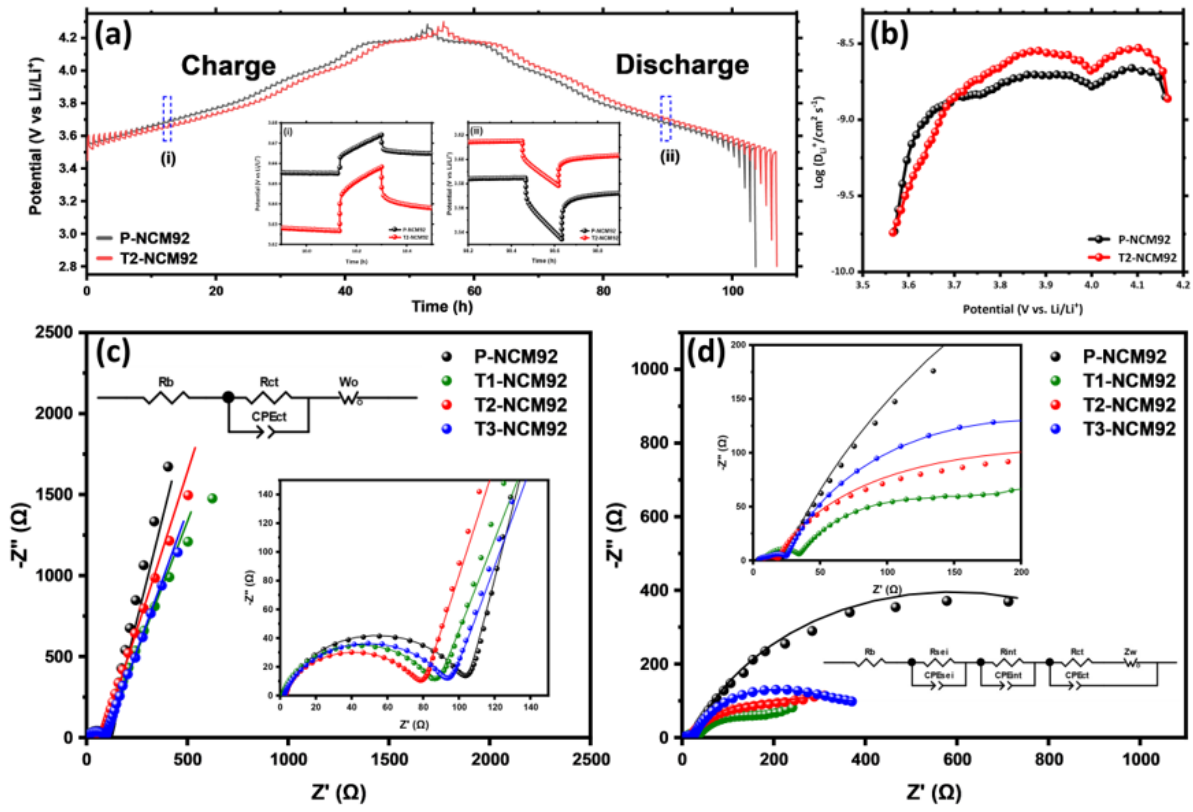

Fig. 10. (a). GITT curves of P-NCM92 and T2-NCM92, (b). Plots of Li^+ ion diffusivity of the electrodes at different potentials, (c,d). AC impedance spectra and equivalent circuit model (the inset) of P-NCM92 and T2-NCM92 samples before cycling and after 200 cycles, respectively (at the C-rates of 1C in the voltage range of 2.8-4.3V at 30°C).

3.6. Post-mortem phase and microstructural Analysis

Post-mortem analyses were used to explore the phase evolution, morphology, and microstructure changes in the P-NCM92 and T2-NCM92 electrodes after long-term cycling (at the C-rates of 1C in the voltage range of 2.8–4.3 V for 200 cycles at 30 °C). Fig. S18a and b show the XRD patterns of the P-NCM92 and T2-NCM92 cathodes before and after 200 cycles, respectively. The peak intensity of both samples deteriorated after 200 cycles, particularly for the P-NCM92, indicating that the structure of the P-NCM92 cathodes substantially deteriorated after 200 cycles, as compared to the T2-NCM92 electrode, which caused the severe capacity fading particularly for extensive cycling (Fig. 8). In addition, the (003) peak of both electrodes shifted towards the small-angle directions as a consequence of the increasing repulsion force between the oxygen-oxygen layers and *c*-axis expansion during the prolonged charge-discharge process [7,53]. However, the deviation angle of the characteristic (003) peak of T2-NCM92 ($\Delta 2\theta$ = 0.16°) sample was lower than that of P-NCM92 ($\Delta 2\theta$ = 0.26°), which confirms that Li^+ ions can be easily reinserted into the structure for the T2-NCM92 electrode, leading to substantially enhanced structural stability.

Fig. S18c and d show the SEM images of the P-NCM92 and T2-NCM92 electrodes after 200 cycles (at 1C in the voltage range of 2.8–4.3 V at 30 °C). After 200 cycles, the structure of the P-NCM92 electrode severely collapsed into the basic primary particle and consisted of significant micro and macrocracks with moderately wide openings. This caused the internal structure to be continuously exposed to liquid electrolytes, and then the erosion prolonged from the surface to the inside, resulting in the pulverization or cracking of numerous particles and preventing the cycling of P-NCM92 (Fig. S18c). By contrast, the T2-NCM92 electrode maintained its original structure even after 200 cycles (Fig. S18d), confirming the synergistic effect of the Ta-enriched phase on the surface with radially aligned primary particles, which can effectively inhibiting infiltration of electrolytes into the particle interior, thereby preventing particle erosion by HF and enhancing the mechanical stability of the electrode.

Furthermore, the chemical composition of the cathode–electrolyte interface (CEI) and mechanism for the improved interfacial stability of the T2-NCM92 electrode were investigated using XPS. The XPS surface analysis was carried out for P-NCM92 and T2-NCM92 electrode after 200 cycles at 1C/1C in the voltage range of 2.8-4.3V, while the corresponding spectra were fitted using the Gaussian-Lorentzian method. The F 1s, C 1s, and O 1s spectrum of the P-NCM92 and T2-NCM92 are shown in Fig. S19. The F 1s spectra peaks are divided into three peaks (Fig. S18a), which correspond to the residual $LiPF_6$ or its reduction products Li_xPF_y (~688 eV), LiF (~685 eV), and $Li_xPO_yF_z$ peaks (~686 eV) [83,84]. The peaks of LiF and $Li_xPO_yF_z$ were generated by electrolyte decomposition (e.g., the side reactions of $LiPF_6$ and H_2O) [26,83,84]. It is observed that the area percentage of LiF was significantly reduced in the T2-NCM92 sample. The area percentage of the LiF is 60.84% for the P-NCM92 and 40.41% for the T2-NCM92. Fig. S19b presents the C 1s spectrum, which were fitted to component adventitious C−C (~285 eV), C-O-C (~286 eV), and O-CO_2 (~288.8 eV). The C−C bonds are related to the binders and conductive substances in the electrode, while C-O-C and O-CO_2 derive from the decomposition of the electrolyte [33,45,84]. The P-NCM92 (*ca.* 19.9%) has a higher area percentage of O-CO_2 than that of T2-NCM92 (*ca.* 13.6%), indicating that electrolyte decomposition forms a thick CEI on the P-NCM92 [26,53,85]. The similar results were further verified from the O 1s spectra (Fig. S19c). The typical peaks of C-O, oxygenated deposited materials, CO_3^{-2}, and electrolyte oxidation appear in the O 1s spectra [84,85]. Its found that the area percentages of electrolyte oxidation and CO_3^{-2} for T2-NCM92 were lower than that of P-NCM92 (Fig. 18c). These observations supported that the Ta-enriched layer on the surface of the T2-NCM92 electrodes effectively inhibited electrolyte decomposition and restrained surface-side reactions [85], as confirmed by Operando Differential Electrochemical Mass Spectroscopy (DEMS) measurements, Fig. S20.

DEMS measurements were performed to evaluate the effectiveness of our coating layer in inhibiting electrolyte decomposition and suppressing outgassing reactions. Fig. S20 presents

the potential profile and the evolved gas (CO_2, $m/z = 44$ and H_2, $m/z = 2$) during the first three cycles in the Li‖P-NCM92 and Li‖T2-NCM92 half-cell using 1 M $LiPF_6$ in ethylene carbonate (EC) and diethyl carbonate (DEC) (1:1, v/v; Aldrich) as electrolyte. It is notable that CO_2 and H_2 evolution is the major gas product from the decomposition of EC-DEC electrolyte [86,87], In both half-cells, CO_2 ($m/z = 44$) release is typically observed at the onset voltage above 4.2 V, and the CO_2 generation was significantly detected at the first cycles, especially for the Li‖T2-NCM92 half-cell. The origin of CO_2 release during cycling might stem from the electrochemical oxidation of the EC-DEC electrolyte, decomposition of residual surface carbonate (Li_2CO_3) on the P-NCM92 [87], and chemical oxidation of the EC-DEC by lattice oxygen release from NCM92 cathode active materials at high voltage [88]. Moreover, H_2 evolution is detected in both samples. Notably, the Li‖T2-NCM92 half-cell releases a lower amount of H_2, as compared to the Li‖P-NCM92 half-cell. H_2 evolution can be caused by the transfer of electrons and H^+ in the EC solvent decomposition and dehydrogenation of the EC components [89]. These results strongly confirmed that Li‖T2-NCM92 half-cell releases much less CO_2 and H_2 gases during the first three cycles, as compared to Li‖P-NCM92 half-cell, indicating that the electrolyte decomposition is suppressed effectively by the coating layer on the surface of the T2-NCM92 cathode active materials.

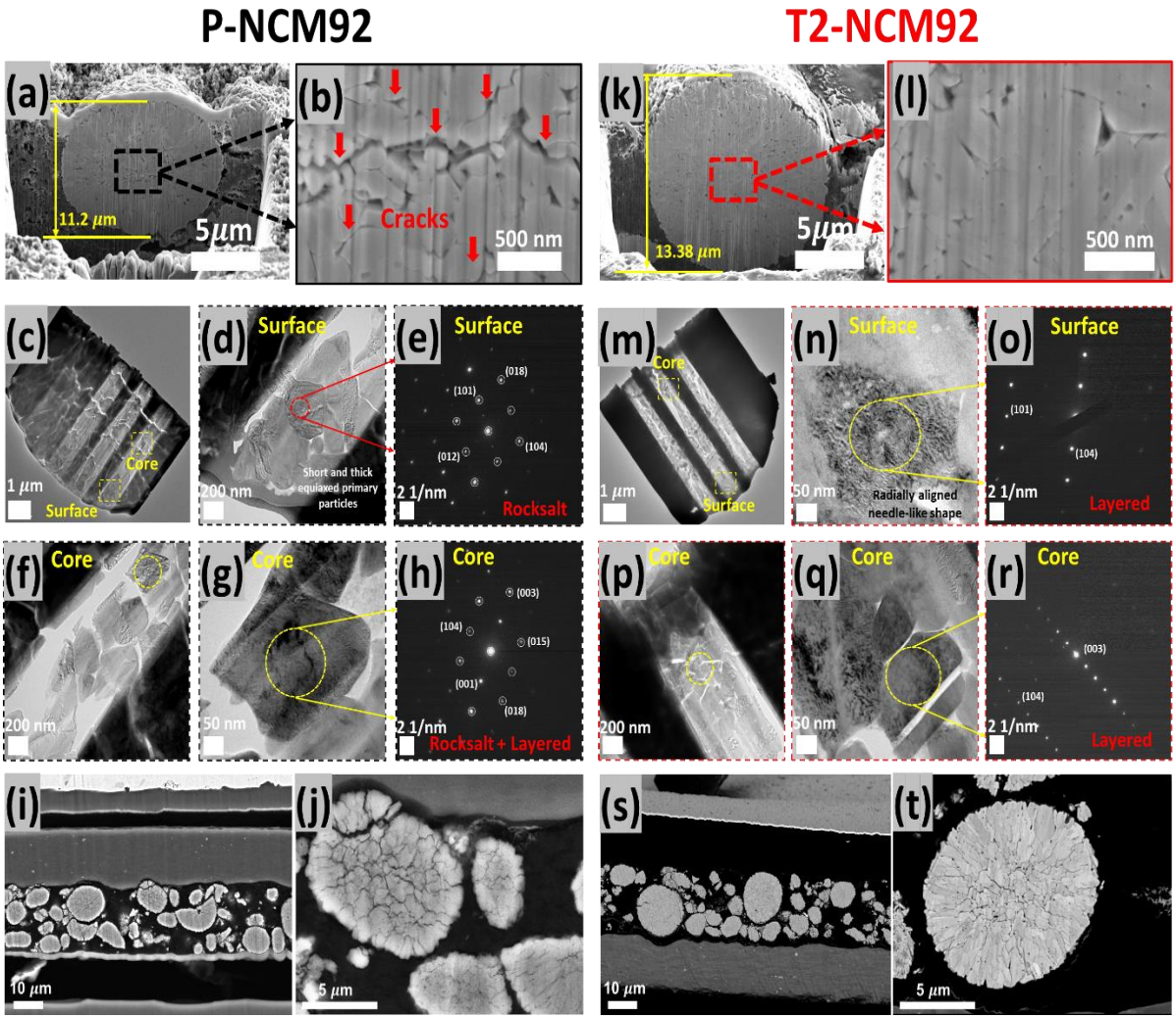

Fig. 11. FIB-SEM images of (a,b). P-NCM92, and (k,l), T2-NCM92 electrodes after 200 cycles at 1C in the voltage range of 2.8-4.3 V; HR-STEM and SAD images at the core and surface region of (c–h) P-NCM92, and (m–r) T2-NCM92 electrodes after 200 cycles at 1C in the voltage range of 2.8-4.3 V; cross-sectional views of (i,j) P-NCM92 and (s,t) T2-NCM92 electrodes after 200 cycles at 1C/1C in the voltage range of 2.8-4.3V

Furthermore, to explicitly observe the difference in microstructure and mechanical stability between the P-NCM92 and T2-NCM92 electrodes after repeated lithiation/delithiation processes for 200 cycles (at 1C in the voltage range of 2.8–4.3 V at 30 °C), FIB-SEM, HR-STEM, and cross-sectional views of P-NCM92 and T2-NCM92 electrodes after 200 cycles were performed (Fig. 11). Notably, the repeated lithiation/delithiation process led to the generation of microcracks in the Ni-rich NCM92 particles owing to volume changes,

originating from H2–H3 transition during cycling, which poses considerable challenges for Ni-rich cathode active materials [49,90].

Fig. 11a and b demonstrate that the P-NCM92 sample contains numerous microcracks with considerable width, particularly at the core. Then, these microcracks propagated to the outer surface of the particles. Conversely, in the case of the T2-NCM92 sample, no notable sign of microcrack nucleation and propagation was observed. Moreover, the presence of microcracks was arrested before propagating to the particle surface. Therefore, the structural integrity was well retained, as shown in Fig. 11k and l. Interestingly, the cross-section view of the P-NCM92 and T2-NCM92 composite electrode shows that the P-NCM92 contains separating primary particles due to the network of the microcracks tracing the interparticle boundaries (Fig. 11i, j), while such microcracks do not visible in T2-NCM92 (Fig. 11s, t).

Furthermore, to determine the reason for the outstanding structural stability of T2-NCM92 cathodes, the HR-STEM and selected area (electron) diffraction (SAD) results were shown in Fig. 11c-h and m-r. The shape and geometric configuration of the primary particles are crucial to relieve the cycling internal strain, arising from anisotropic volume change during lithiation/delithiation [54,58]. Fig. 11c and d illustrate that the P-NCM92 sample was randomly oriented with short, thick equiaxed primary particles, as comparable to the uncycled state in Fig. 2. This configuration easily generates local stress concentration and stimulates anisotropic volume change, initiating nucleation and microcrack propagation at the boundaries and separating the primary particles [41,91]. By contrast, Fig. 11m and n show that the T2-NCM92 sample exhibited a thin, elongated, and tightly packed structure along the radial directions of primary particles (comparable to the uncycled state in Fig. 2). This structure allows the anisotropic strain to be effectively absorbed and contract uniformly in the secondary particle without any local stress, which is beneficial to suppress the microcrack formation [41]. In addition, the structure and phase transformation starting from the surface to the inner bulk of

the cathodes after long-term cycling were examined using HR-STEM-SAD (Fig. 11d-h for P-NCM92, and 11n-r for T2-NCM92) and HR-TEM-SAD (Fig. S21). The results demonstrated that after long-term cycling at 1C, the surface and inner bulk of the T2-NCM92 electrode maintained the original layered structure (R-$\bar{3}$m). However, the P-NCM92 electrodes show the appearance of the rock-salt phase (Fm-$\bar{3}$m) on its surface, and an R-$\bar{3}$m and Fm-$\bar{3}$m mix-phase in the inner bulk of the particles. The transformation from layered structure (R-$\bar{3}$m) and eventually to the rock-salt-mixed and rock-salt structure (Fm-$\bar{3}$m) in the P-NCM92 sample is attributed to the Li^+/Ni^{2+} cation mixing disorder and lattice oxygen loss, which is accelerated at high Ni-content [10,41]. Notably, the non-electrochemically active rock-salt phase on the cathode active materials might block the Li^+ ion diffusion path, reduce ionic conductivity, and trigger rapid electrode degradation [41,92]. Moreover, the HR-STEM-EDS was performed on the T2-NCM92 electrode after long-term cycling (Fig. S22). The results show the presence of the Ta signal, which suggests that Ta^{5+} diffused into the inside particles along the grain boundaries during cycling.

4. Conclusions

The Ta modification of Ni-rich NCM (Tx-NCM92) improves its electrochemical properties and ensures long-term cycling stability. In comparison to P-NCM92, excellent long-term cycling stability was particularly evident under harsh cycling conditions, such as elevated temperature, high cut-off voltage, fast cycling, and extensive cycling. This excellent stability was achieved because Ta is a dopant and coating agent on the primary particles that alters the microstructure, orientation, and morphology of the primary NCM92 particles into a radially aligned needle-like shape with fine structures. This structure is beneficial for the fast transport of Li^+ ions and their electrochemical stability. In addition, Ta can form a surface-coating layer on secondary particles, effectively suppressing microcrack formation, inhibiting electrolyte decomposition, and restraining surface side reactions during cycling. The charge-discharge test

showed that the T2-NCM92 electrode provided a capacity retention of approximately 84.5% after 200 cycles at 1C. By contrast, the P-NCM92 electrode delivers a much inferior capacity retention of only 55.3% over the same cycling period. In addition, the T2-NCM92 electrode provides capacity retention of 78.3% at 4.5 V and 67.6% at 45 ℃ after 200 cycles at 1C. In comparison, the discharge capacity retention of the P-NCM92 electrode is only 53.9% at 4.5 V and 78.3% at 45℃ over the same cycling periods. In addition, the Li^+ ion diffusion coefficient (D_{Li^+}) of the T2-NCM electrode was two orders of magnitude higher than that of the P-NCM92 electrode, which is beneficial for high C-rate performance. DFT was applied to simulate the aforementioned doping effects of Ta^{5+} on NCM92 as a dopant and surface-coating agent, which was fully consistent with our experimental observations. Therefore, Ta-modified Ni-rich NCM is a promising candidate for fabricating future high-energy LIBs in EV applications.

Acknowledgements

This research is supported by the Ministry of Science and Technology, Taiwan (Project No: MOST 108-2221-E-131-002-MY3, MOST 111-2221-E-131-003 and MOST 111-2222-E-131-002) The Alexander-von-Humboldt Foundation (Grant No.: 112-2927-I-011-505), Bundesministerium für Bildung und Forschung (BMBF), and the Taiwanese National Science and Technology Council. Special appreciation for the scientific services with the FIB system along with FE–SEM/EDS and HR-TEM-EDS-SAED at High–Resolution Analytical Instrumentation Center at National Central University. Computing time was granted through JARA-HPC on the supercomputer JURECA at Forschungszentrum Jülich in Germany.

References

[1] G. Xu, X. Liu, A. Daali, R. Amine, Z. Chen, K. Amine, Challenges and strategies to advance high- energy nickel- rich layered lithium transition metal oxide cathodes for harsh operation, Adv. Funct. Mater. 30 (2020) 2004748.

[2] W. Yan, S. Yang, Y. Huang, Y. Yang, G. Yuan, A review on doping/coating of nickel-rich cathode materials for lithium-ion batteries, J. Alloys Compd. 819 (2020) 153048.

[3] L. Qiu, M. Zhang, Y. Song, Y. Xiao, Z. Wu, W. Xiang, Y. Liu, G. Wang, Y. Sun, J. Zhang, Recent advance in structure regulation of high- capacity Ni- rich layered oxide cathodes, EcoMat. 3 (2021) e12141.

[4] A. Manthiram, B. Song, W. Li, A perspective on nickel-rich layered oxide cathodes for lithium-ion batteries, Energy Storage Mater. 6 (2017) 125–139.

[5] M. Malik, K.H. Chan, G. Azimi, Review on the synthesis of LiNixMnyCo1-x-yO2 (NMC) cathodes for lithium-ion batteries, Mater. Today Energy. 28 (2022) 101066.

[6] Y. Lu, Y. Zhang, Q. Zhang, F. Cheng, J. Chen, Recent advances in Ni-rich layered oxide particle materials for lithium-ion batteries, Particuology. 53 (2020) 1–11.

[7] A. Chakraborty, S. Kunnikuruvan, M. Dixit, D.T. Major, Review of Computational Studies of NCM Cathode Materials for Li- ion Batteries, Isr. J. Chem. 60 (2020) 850–862.

[8] T. Mueller, G. Hautier, A. Jain, G. Ceder, Evaluation of tavorite-structured cathode materials for lithium-ion batteries using high-throughput computing, Chem. Mater. 23 (2011) 3854–3862.

[9] H.-H. Ryu, N.-Y. Park, T.-C. Noh, G.-C. Kang, F. Maglia, S.-J. Kim, C.S. Yoon, Y.-K. Sun, Microstrain alleviation in high-energy Ni-rich NCMA cathode for long battery life, ACS Energy Lett. 6 (2020) 216–223.

[10] M. Jiang, D.L. Danilov, R. Eichel, P.H.L. Notten, A review of degradation mechanisms and recent achievements for Ni- rich cathode- based Li- ion batteries, Adv. Energy Mater. 11 (2021) 2103005.

[11] A. Aishova, G.T. Park, C.S. Yoon, Y.K. Sun, Cobalt-Free High-Capacity Ni-Rich Layered Li[Ni0.9Mn0.1]O2 Cathode, Adv. Energy Mater. 10 (2020) 1–9. https://doi.org/10.1002/aenm.201903179.

[12] C. Wang, L. Tan, H. Yi, Z. Zhao, X. Yi, Y. Zhou, J. Zheng, J. Wang, L. Li, Unveiling the impact of residual Li conversion and cation ordering on electrochemical performance of Co-free Ni-rich cathodes, Nano Res. 15 (2022) 9038–9046.

[13] Y. Lin, C.M. Abram, X. Shi, I.G. McKendry, Z. Wang, H. Zhong, H. Zhao, X. Yang, B.E. Koel, C. Yan, Enhanced Thermal Stability of Aerosol-Synthesized Ni-Rich Li-Ion Battery Cathode Materials via Concentration-Gradient Ca Doping, ACS Appl. Energy Mater. 5 (2022) 10751–10757.

[14] M. Akhilash, P.S. Salini, B. John, S. Sujatha, T.D. Mercy, Surface Modification on Nickel rich Cathode Materials for Lithium- Ion Cells: A Mini Review, Chem. Rec. (2023) e202300132.

[15] L. Li, L. Fu, M. Li, C. Wang, Z. Zhao, S. Xie, H. Lin, X. Wu, H. Liu, L. Zhang, B-doped and La4NiLiO8-coated Ni-rich cathode with enhanced structural and interfacial stability for lithium-ion batteries, J. Energy Chem. 71 (2022) 588–594.

[16] Z. Wang, H. Zhu, H. Yu, T. Zhang, Y. Hu, H. Jiang, C. Li, Complementary dual-doping of LiNi0. 8Co0. 1Mn0. 1O2 cathode enhances ion-diffusion and stability for Li-ion batteries, Chinese Chem. Lett. 34 (2023) 107718.

[17] U.-H. Kim, N.-Y. Park, G.-T. Park, H. Kim, C.S. Yoon, Y.-K. Sun, High-energy W-doped Li [Ni0. 95Co0. 04Al0. 01] O2 cathodes for next-generation electric vehicles, Energy Storage Mater. 33 (2020) 399–407.

[18] Z. Ahaliabadeh, X. Kong, E. Fedorovskaya, T. Kallio, Extensive comparison of doping and coating strategies for Ni-rich positive electrode materials, J. Power Sources. 540 (2022) 231633.

[19] H.H. Sun, U.-H. Kim, J.-H. Park, S.-W. Park, D.-H. Seo, A. Heller, C.B. Mullins, C.S. Yoon, Y.-K. Sun, Transition metal-doped Ni-rich layered cathode materials for durable

Li-ion batteries, Nat. Commun. 12 (2021) 6552.

[20] S.S. Zhang, Problems and their origins of Ni-rich layered oxide cathode materials, Energy Storage Mater. 24 (2020) 247–254.

[21] H. Ryu, N. Park, D.R. Yoon, U. Kim, C.S. Yoon, Y. Sun, New class of Ni- rich cathode materials Li [NixCoyB1− x− y] O2 for next lithium batteries, Adv. Energy Mater. 10 (2020) 2000495.

[22] K. Park, H. Jung, L. Kuo, P. Kaghazchi, C.S. Yoon, Y. Sun, Improved cycling stability of Li [Ni0. 90Co0. 05Mn0. 05] O2 through microstructure modification by boron doping for Li- ion batteries, Adv. Energy Mater. 8 (2018) 1801202.

[23] T.T. Nguyen, U.-H. Kim, C.S. Yoon, Y.-K. Sun, Enhanced cycling stability of Sn-doped Li [Ni0. 90Co0. 05Mn0. 05] O2 via optimization of particle shape and orientation, Chem. Eng. J. 405 (2021) 126887.

[24] D. Kim, J. Song, C. Jung, D. Eum, B. Kim, S. Hong, K. Kang, Stepwise dopant selection process for high- nickel layered oxide cathodes, Adv. Energy Mater. 12 (2022) 2200136.

[25] Y.-R. Luo, J.A. Kerr, Bond dissociation energies, CRC Handb. Chem. Phys. 89 (2012) 89.

[26] S. Jamil, R. Yu, Q. Wang, M. Fasehullah, Y. Huang, Z. Yang, X. Yang, X. Wang, Enhanced cycling stability of nickel-rich layered oxide by tantalum doping, J. Power Sources. 473 (2020) 228597. https://doi.org/https://doi.org/10.1016/j.jpowsour.2020.228597.

[27] W. Li, S. Lee, A. Manthiram, High-Nickel NMA: A Cobalt-Free Alternative to NMC and NCA Cathodes for Lithium-Ion Batteries, Adv. Mater. 32 (2020). https://doi.org/10.1002/adma.202002718.

[28] T.A. Saleh, Chapter 7 - Structural characterization of hybrid materials, in: T.A.B.T.-P.H.M. and N. Saleh (Ed.), Plast. Des. Libr., William Andrew Publishing, 2021: pp. 213–240. https://doi.org/https://doi.org/10.1016/B978-0-12-813294-4.00005-4.

[29] P.E. Blöchl, Projector augmented-wave method, Phys. Rev. B. 50 (1994) 17953.

[30] G. Kresse, J. Furthmüller, Efficient iterative schemes for ab initio total-energy calculations using a plane-wave basis set, Phys. Rev. B. 54 (1996) 11169.

[31] J.P. Perdew, K. Burke, M. Ernzerhof, Generalized gradient approximation made simple, Phys. Rev. Lett. 77 (1996) 3865.

[32] K. Momma, F. Izumi, VESTA 3 for three-dimensional visualization of crystal, volumetric and morphology data, J. Appl. Crystallogr. 44 (2011) 1272–1276.

[33] W. Yang, H. Li, D. Wang, C. Xu, W. Xiang, Y. Song, F. He, J. Zhang, B. Zheng, B. Zhong, Z. Wu, X. Guo, Ta induced fine tuning of microstructure and interface enabling Ni-rich cathode with unexpected cyclability in pouch-type full cell, Nano Energy. 104 (2022) 107880. https://doi.org/https://doi.org/10.1016/j.nanoen.2022.107880.

[34] B.T. Truong, Y.-S. Wu, T.-F. Hung, W.-C. Chien, S.-H. Wu, R. Jose, S.J. Lue, C.-C. Yang, The effect of lithium-excess on Ni-rich LiNi0. 6Co0. 2Mn0. 2O2 cathode materials prepared by a Taylor flow reactor, Electrochim. Acta. 391 (2021) 138982.

[35] E.B. Abebe, C.-C. Yang, S.-H. Wu, W.-C. Chien, Y.-J.J. Li, Effect of Li excess on electrochemical performance of Ni-rich LiNi0. 9Co0. 05Mn0. 05O2 cathode materials

for Li-ion batteries, ACS Appl. Energy Mater. 4 (2021) 14295–14308.

[36] T.-Y. Zeng, X.-Y. Zhang, X.-Y. Qu, M.-Q. Li, P.-P. Zhang, M.-R. Su, A.-C. Dou, A. Naveed, Y. Zhou, Y.-J. Liu, Mechanism exploration of enhanced electrochemical performance of single-crystal versus polycrystalline LiNi0.8Mn0.1Co0.1O2, Rare Met. 41 (2022) 3783–3794. https://doi.org/10.1007/s12598-022-02055-5.

[37] M. Seenivasan, C.-C. Yang, S. Wu, W.-C. Chien, Y.-S. Wu, R. Jose, S.J. Lue, Using a Couette–Taylor vortex flow reactor to prepare a uniform and highly stable Li [Ni0· 80Co0· 15Al0. 05] O2 cathode material, J. Alloys Compd. 857 (2021) 157594.

[38] Y. Qu, W. Zhou, X. Miao, Y. Li, L. Jiang, K. Pan, G. Tian, Z. Ren, G. Wang, H. Fu, A New Layered Photocathode with Porous NiO Nanosheets: An Effective Candidate for p- Type Dye- Sensitized Solar Cells, Chem. Asian J. 8 (2013) 3085–3090.

[39] L. Qiu, M. Zhang, Y. Ming, Y. Song, C. Xu, Z. Wu, Q. Xu, T. Chen, G. Wang, Y. Liu, Exposing microstructure evolution of Ni-Rich Ni-Co-Al hydroxide precursor, Chem. Eng. Sci. 233 (2021) 116337.

[40] L.M. Babulal, C. Yang, S. Wu, W.-C. Chien, R. Jose, S.J. Lue, Enhanced performance of a Ni-rich LiNi0. 8Co0. 1Mn0. 1O2 cathode material formed through Taylor flow synthesis and surface modification with Li2MoO4, Chem. Eng. J. 413 (2021) 127150.

[41] S. Yin, W. Deng, J. Chen, X. Gao, G. Zou, H. Hou, X. Ji, Fundamental and solutions of microcrack in Ni-rich layered oxide cathode materials of lithium-ion batteries, Nano Energy. 83 (2021) 105854. https://doi.org/https://doi.org/10.1016/j.nanoen.2021.105854.

[42] B. Du, Y. Mo, H. Jin, X. Li, Y. Qu, D. Li, B. Cao, X. Jia, Y. Lu, Y. Chen, Radially microstructural design of LiNi0. 8Co0. 1Mn0. 1O2 cathode material toward long-term cyclability and high rate capability at high voltage, ACS Appl. Energy Mater. 3 (2020) 6657–6669.

[43] Y.S. Kim, J.H. Kim, Y.-K. Sun, C.S. Yoon, Evolution of a radially aligned microstructure in boron-doped Li [Ni0. 95Co0. 04Al0. 01] O2 cathode particles, ACS Appl. Mater. Interfaces. 14 (2022) 17500–17508.

[44] N. Park, S. Kim, M. Kim, S. Han, D. Kim, M. Kim, Y. Sun, Mechanism of Doping with High- Valence Elements for Developing Ni- Rich Cathode Materials, Adv. Energy Mater. 13 (2023) 2301530.

[45] X. Li, W. Ge, K. Zhang, G. Peng, Y. Fu, X. Ma, Comprehensive study of tantalum doping on morphology, structure, and electrochemical performance of Ni-rich cathode materials, Electrochim. Acta. 403 (2022) 139653. https://doi.org/https://doi.org/10.1016/j.electacta.2021.139653.

[46] I. Petousis, D. Mrdjenovich, E. Ballouz, M. Liu, D. Winston, W. Chen, T. Graf, T.D. Schladt, K.A. Persson, F.B. Prinz, High-throughput screening of inorganic compounds for the discovery of novel dielectric and optical materials, Sci. Data. 4 (2017) 1–12.

[47] J. Shi, Z. Ma, K. Han, Q. Wan, D. Wu, X. Qu, P. Li, Coupling novel Li7TaO6 surface buffering with bulk Ta-doping to achieve long-life sulfide-based all-solid-state lithium batteries, J. Mater. Chem. A. 10 (2022) 21336–21348. https://doi.org/10.1039/D2TA06703J.

[48] Y. Chen, Y. Yan, J. Wu, C. Wang, J.Y. Lin, J.S. Zhao, C.S. Hwang, Electroforming-free, flexible, and reliable resistive random-access memory based on an ultrathin TaO x film, ACS Appl. Mater. Interfaces. 12 (2020) 10681–10688.

[49] K. Park, J.-H. Park, S.-G. Hong, B. Choi, S.-W. Seo, J.-H. Park, K. Min, Enhancement in the electrochemical performance of zirconium/phosphate bi-functional coatings on LiNi0.8Co0.15Mn0.05O2 by the removal of Li residuals, Phys. Chem. Chem. Phys. 18 (2016) 29076–29085. https://doi.org/10.1039/C6CP05286J.

[50] B. Huang, D. Liu, K. Qian, L. Zhang, K. Zhou, Y. Liu, F. Kang, B. Li, A Simple Method for the Complete Performance Recovery of Degraded Ni-rich LiNi0.70Co0.15Mn0.15O2 Cathode via Surface Reconstruction, ACS Appl. Mater. Interfaces. 11 (2019) 14076–14084. https://doi.org/10.1021/acsami.8b22529.

[51] N. Wu, H. Wu, J. Kim, X. Liu, Y. Zhang, Restoration of Degraded Nickel- Rich Cathode Materials for Long- Life Lithium- Ion Batteries, ChemElectroChem. 5 (2018) 78–83.

[52] P. Zhang, Z. Liu, B. Ma, P. Li, Y. Zhou, X. Tian, Improving the single crystal LiNi0. 8Co0. 1Mn0. 1O2 cathode material performance by fluorine doping, Ceram. Int. 47 (2021) 33843–33852.

[53] Z. Guo, Z. Jian, S. Zhang, Y. Feng, W. Kou, H. Ji, G. Yang, The effect of Ni oxidation state on the crystal structure and electrochemical properties of LiNi0.8Co0.1Mn0.1O2 cathode material for highly reversible lithium storage, J. Alloys Compd. 882 (2021) 160642. https://doi.org/https://doi.org/10.1016/j.jallcom.2021.160642.

[54] Y. Liu, X. Fan, B. Luo, Z. Zhao, J. Shen, Z. Liu, Z. Xiao, B. Zhang, J. Zhang, L. Ming, X. Ou, Understanding the enhancement effect of boron doping on the electrochemical performance of single-crystalline Ni-rich cathode materials, J. Colloid Interface Sci. 604 (2021) 776–784. https://doi.org/https://doi.org/10.1016/j.jcis.2021.07.027.

[55] J. Li, W. Zhong, Q. Deng, Q. Zhang, Z. Lin, C. Yang, Mechanistic Origin for High Structural Stability of Single Crystalline Nickel- Rich Cathode Materials Via Al and Sm Co- Doping, Adv. Funct. Mater. 33 (2023) 2300127.

[56] Q. Ran, H. Zhao, Q. Wang, X. Shu, Y. Hu, S. Hao, M. Wang, J. Liu, M. Zhang, H. Li, N. Liu, X. Liu, Dual functions of gradient phosphate polyanion doping on improving the electrochemical performance of Ni-rich LiNi0.6Co0.2Mn0.2O2 cathode at high cut-off voltage and high temperature, Electrochim. Acta. 299 (2019) 971–978. https://doi.org/https://doi.org/10.1016/j.electacta.2019.01.082.

[57] M. Li, J. Lu, Cobalt in lithium-ion batteries, Science (80-.). 367 (2020) 979–980. https://doi.org/10.1126/science.aba9168.

[58] S.-J. Sim, S.-H. Lee, B.-S. Jin, H.-S. Kim, Effects of lithium tungsten oxide coating on LiNi0.90Co0.05Mn0.05O2 cathode material for lithium-ion batteries, J. Power Sources. 481 (2021) 229037. https://doi.org/https://doi.org/10.1016/j.jpowsour.2020.229037.

[59] L. Kahle, X. Cheng, T. Binninger, S.D. Lacey, A. Marcolongo, F. Zipoli, E. Gilardi, C. Villevieille, M. El Kazzi, N. Marzari, The solid-state Li-ion conductor Li7TaO6: A combined computational and experimental study, Solid State Ionics. 347 (2020) 115226.

[60] U.-H. Kim, G.-T. Park, B.-K. Son, G.W. Nam, J. Liu, L.-Y. Kuo, P. Kaghazchi, C.S. Yoon, Y.-K. Sun, Heuristic solution for achieving long-term cycle stability for Ni-rich layered cathodes at full depth of discharge, Nat. Energy. 5 (2020) 860–869.

[61] X. He, H. Sun, X. Ding, K. Zhao, Grain boundaries and their impact on Li kinetics in layered-oxide cathodes for Li-ion batteries, J. Phys. Chem. C. 125 (2021) 10284–10294.

[62] N. Zaker, C. Geng, D. Rathore, I. Hamam, N. Chen, P. Xiao, C. Yang, J.R. Dahn, G.A. Botton, Probing the Mysterious Behavior of Tungsten as a Dopant Inside Pristine

Cobalt- Free Nickel- Rich Cathode Materials, Adv. Funct. Mater. (2023) 2211178.

[63] C. Geng, D. Rathore, D. Heino, N. Zhang, I. Hamam, N. Zaker, G.A. Botton, R. Omessi, N. Phattharasupakun, T. Bond, Mechanism of action of the tungsten dopant in LiNiO2 positive electrode materials, Adv. Energy Mater. 12 (2022) 2103067.

[64] D. Rathore, C. Geng, N. Zaker, I. Hamam, Y. Liu, P. Xiao, G.A. Botton, J. Dahn, C. Yang, Tungsten infused grain boundaries enabling universal performance enhancement of Co-free Ni-rich cathode materials, J. Electrochem. Soc. 168 (2021) 120514.

[65] Y. Liu, W. Che, D. Gao, D. Zhang, C. Chang, Ta Doping Improves the Cyclability and Rate Performance of a Nickel-Rich NCA Cathode via Promoted Electronic and Cationic Conductivity, ACS Sustain. Chem. Eng. 10 (2022) 16516–16526.

[66] C.-H. Jung, Q. Li, D.-H. Kim, D. Eum, D. Ko, J. Choi, J. Lee, K.-H. Kim, K. Kang, W. Yang, Revisiting the role of Zr doping in Ni-rich layered cathodes for lithium-ion batteries, J. Mater. Chem. A. 9 (2021) 17415–17424.

[67] C. Zhu, M. Cao, H. Zhang, G. Lv, J. Zhang, Y. Meng, C. Shu, W. Fan, M. Zuo, W. Xiang, Synergistic effect of microstructure engineering and local crystal structure tuning to improve the cycling stability of Ni-rich cathodes, ACS Appl. Mater. Interfaces. 13 (2021) 48720–48729.

[68] Z. Qiu, Y. Zhang, Z. Liu, Y. Gao, J. Liu, Q. Zeng, Stabilizing Ni- Rich LiNi0. 92Co0. 06Al0. 02O2 Cathodes by Boracic Polyanion and Tungsten Cation Co- Doping for High- Energy Lithium- Ion Batteries, ChemElectroChem. 7 (2020) 3811–3817.

[69] H.-H. Ryu, S.-B. Lee, Y.-K. Sun, Promoting grain growth in Ni-rich single-crystal cathodes for high-performance lithium-ion batteries through Ce doping, J. Solid State Electrochem. 26 (2022) 2097–2105.

[70] J. Jeyakumar, Y.-S. Wu, S.-H. Wu, R. Jose, C.-C. Yang, Surface-Modified Quaternary Layered Ni-Rich Cathode Materials by Li2ZrO3 for Improved Electrochemical Performance for High-Power Li-Ion Batteries, ACS Appl. Energy Mater. 5 (2022) 4796–4807.

[71] H. Ding, M. Fang, Y. Li, L. Huang, C. Zhang, X. Luo, Enhanced lithium storage capability of Ni-rich LiNi0. 9CoxMn0. 1− xO2 (0≤ x≤ 0.1) cathode by co-operation of Al-doping and V-coating, J. Alloys Compd. 946 (2023) 169428.

[72] A. Banday, M. Ali, R. Pandey, S. Murugavel, Direct evidence for the influence of lithium ion vacancies on polaron transport in nanoscale LiFePO4, Phys. Chem. Chem. Phys. 21 (2019) 9858–9864. https://doi.org/10.1039/C9CP00408D.

[73] R. Qian, Y. Liu, T. Cheng, P. Li, R. Chen, Y. Lyu, B. Guo, Enhanced surface chemical and structural stability of Ni-rich cathode materials by synchronous lithium-ion conductor coating for lithium-ion batteries, ACS Appl. Mater. Interfaces. 12 (2020) 13813–13823.

[74] M. Dixit, B. Markovsky, F. Schipper, D. Aurbach, D.T. Major, Origin of structural degradation during cycling and low thermal stability of Ni-rich layered transition metal-based electrode materials, J. Phys. Chem. C. 121 (2017) 22628–22636.

[75] M. Eilers-Rethwisch, M. Winter, F.M. Schappacher, Synthesis, electrochemical investigation and structural analysis of doped Li [Ni0. 6Mn0. 2Co0. 2-xMx] O2 (x= 0, 0.05; M= Al, Fe, Sn) cathode materials, J. Power Sources. 387 (2018) 101–107.

[76] T. Weigel, F. Schipper, E.M. Erickson, F.A. Susai, B. Markovsky, D. Aurbach, Structural and electrochemical aspects of LiNi0. 8Co0. 1Mn0. 1O2 cathode materials doped by various cations, ACS Energy Lett. 4 (2019) 508–516.

[77] H. Li, A. Liu, N. Zhang, Y. Wang, S. Yin, H. Wu, J.R. Dahn, An unavoidable challenge for Ni-rich positive electrode materials for lithium-ion batteries, Chem. Mater. 31 (2019) 7574–7583.

[78] Y. Han, S. Heng, Y. Wang, Q. Qu, H. Zheng, Anchoring interfacial nickel cations on single-crystal LiNi0. 8Co0. 1Mn0. 1O2 cathode surface via controllable electron transfer, ACS Energy Lett. 5 (2020) 2421–2433.

[79] J. Hwang, K. Do, H. Ahn, Highly conductive 3D structural carbon network-encapsulated Ni-rich LiNi0. 8Co0. 1Mn0. 1O2 as depolarized and passivated cathode for lithium-ion batteries, Chem. Eng. J. 406 (2021) 126813.

[80] R. Ma, Z. Zhao, J. Fu, H. Lv, C. Li, B. Wu, D. Mu, F. Wu, Tuning Cobalt-Free Nickel-Rich Layered LiNi0.9Mn0.1O2 Cathode Material for Lithium-Ion Batteries, ChemElectroChem. 7 (2020) 2637–2642. https://doi.org/10.1002/celc.202000443.

[81] A. Liu, N. Zhang, H. Li, J. Inglis, Y. Wang, S. Yin, H. Wu, J.R. Dahn, Investigating the Effects of Magnesium Doping in Various Ni-Rich Positive Electrode Materials for Lithium Ion Batteries, J. Electrochem. Soc. 166 (2019) A4025–A4033. https://doi.org/10.1149/2.1101915jes.

[82] J. Hu, L. Zhang, S. Zhong, Z. Li, M. Zeng, F. Fan, T. Yan, Extended fast-charging life of ultrahigh-Ni layered oxides by adjusting the current density during the H2→ H3 phase transition, Energy Storage Mater. 50 (2022) 751–759.

[83] P. Guan, L. Liu, X. Lin, Simulation and experiment on solid electrolyte interphase (SEI) morphology evolution and lithium-ion diffusion, J. Electrochem. Soc. 162 (2015) A1798.

[84] R. Tatara, P. Karayaylali, Y. Yu, Y. Zhang, L. Giordano, F. Maglia, R. Jung, J.P. Schmidt, I. Lund, Y. Shao-Horn, The effect of electrode-electrolyte interface on the electrochemical impedance spectra for positive electrode in Li-ion battery, J. Electrochem. Soc. 166 (2019) A5090–A5098.

[85] L. Wang, Y. Chu, Y. Nong, F. Zheng, Y. Li, Y. Huang, Y. Li, Q. Pan, H. Wang, Q. Li, Sr-Based Sub/Surface Integrated Layer and Bulk Doping to Enhance High-Voltage Cycling of a Ni-Rich Cathode Material, ACS Sustain. Chem. Eng. 10 (2022) 7883–7895.

[86] X. Teng, C. Zhan, Y. Bai, L. Ma, Q. Liu, C. Wu, F. Wu, Y. Yang, J. Lu, K. Amine, In situ analysis of gas generation in lithium-ion batteries with different carbonate-based electrolytes, ACS Appl. Mater. Interfaces. 7 (2015) 22751–22755.

[87] J.H. Teo, F. Strauss, Đ. Tripković, S. Schweidler, Y. Ma, M. Bianchini, J. Janek, T. Brezesinski, Design-of-experiments-guided optimization of slurry-cast cathodes for solid-state batteries, Cell Reports Phys. Sci. 2 (2021).

[88] T. Hatsukade, A. Schiele, P. Hartmann, T. Brezesinski, J. Janek, Origin of carbon dioxide evolved during cycling of nickel-rich layered NCM cathodes, ACS Appl. Mater. Interfaces. 10 (2018) 38892–38899.

[89] T. Kocak, L. Wu, A. Ugur, L. Shen, F. De Giorgio, M. Kunduraci, X. Zhang, Effect of doping amount on capacity retention and electrolyte decomposition of LiNi0. 5Mn1. 5O4-based cathode at high temperature, J. Solid State Chem. 310 (2022) 123006.

[90] Y. Kim, W.M. Seong, A. Manthiram, Cobalt-free, high-nickel layered oxide cathodes for lithium-ion batteries: Progress, challenges, and perspectives, Energy Storage Mater. 34 (2021) 250–259. https://doi.org/10.1016/j.ensm.2020.09.020.

[91] M. Campanati, G. Fornasari, A. Vaccari, Fundamentals in the preparation of heterogeneous catalysts, Catal. Today. 77 (2003) 299–314.

[92] B. Zhu, Z. Yu, L. Meng, Z. Xu, C. Lv, Y. Wang, G. Wei, J. Qu, The relationship between failure mechanism of nickel-rich layered oxide for lithium batteries and the research progress of coping strategies: a review, Ionics (Kiel). 27 (2021) 2749–2784.